Monthly Notices
of the
ROYAL ASTRONOMICAL SOCIETY

MNRAS **506,** 4083–4100 (2021)
Advance Access publication 2021 July 8

https://doi.org/10.1093/mnras/stab1920

The loudest stellar heartbeat: characterizing the most extreme amplitude heartbeat star system

T. Jayasinghe [1,2]★ C. S. Kochanek,[1,2] J. Strader,[3] K. Z. Stanek,[1,2] P. J. Vallely,[1,2] Todd A. Thompson [1,2] J. T. Hinkle [4] B. J. Shappee,[4] A. K. Dupree,[5] K. Auchettl,[6,7,8] L. Chomiuk,[3] E. Aydi,[3] K. Dage,[3,9,10] A. Hughes,[11] L. Shishkovsky,[3] K. V. Sokolovsky [3,12] S. Swihart,[3,13]† K. T. Voggel[14] and I. B. Thompson[15]

[1]*Department of Astronomy, The Ohio State University, 140 West 18th Avenue, Columbus, OH 43210, USA*
[2]*Center for Cosmology and Astroparticle Physics, The Ohio State University, 191 W. Woodruff Avenue, Columbus, OH 43210, USA*
[3]*Center for Data Intensive and Time Domain Astronomy, Department of Physics and Astronomy, Michigan State University, East Lansing, MI 48824, USA*
[4]*Institute for Astronomy, University of Hawaii, 2680 Woodlawn Drive, Honolulu, HI 96822, USA*
[5]*Center for Astrophysics, Harvard & Smithsonian, 60 Garden Street, MS-15, Cambridge, MA 02138, USA*
[6]*School of Physics, The University of Melbourne, Parkville, VIC 3010, Australia*
[7]*ARC Centre of Excellence for All Sky Astrophysics in 3 Dimensions (ASTRO 3D), Australia*
[8]*Department of Astronomy and Astrophysics, University of California, Santa Cruz, CA 95064, USA*
[9]*Department of Physics, McGill University, 3600 University Street, Montréal, QC H3A 2T8, Canada*
[10]*McGill Space Institute, McGill University, 3550 University Street, Montréal, QC H3A 2A7, Canada*
[11]*Department of Astronomy/Steward Observatory, 933 North Cherry Avenue, Rm. N204, Tucson, AZ 85721-0065, USA*
[12]*Sternberg Astronomical Institute, Moscow State University, Universitetskii pr. 13, 119992 Moscow, Russia*
[13]*National Research Council Research Associate, National Academy of Sciences, Washington, DC 20001, USA*
[14]*Universite de Strasbourg, CNRS, Observatoire Astronomique de Strasbourg, UMR 7550, F-67000 Strasbourg, France*
[15]*Carnegie Observatories, 813 Santa Barbara Street, Pasadena, CA 91101-1292, USA*

Accepted 2021 June 30. Received 2021 June 29; in original form 2021 April 28

ABSTRACT

We characterize the extreme heartbeat star system MACHO 80.7443.1718 in the Large Magellanic Cloud using Transiting Exoplanet Survey Satellite (*TESS*) photometry and spectroscopic observations from the Magellan Inamori Kyocera Echelle (MIKE) and SOAR Goodman spectographs. MACHO 80.7443.1718 was first identified as a heartbeat star system in the All-Sky Automated Survey for SuperNovae (ASAS-SN) with $P_{\rm orb} = 32.836 \pm 0.008$ d. MACHO 80.7443.1718 is a young (∼6 Myr), massive binary, composed of a B0 Iae supergiant with $M_1 \simeq 35\,{\rm M}_\odot$ and an O9.5V secondary with $M_2 \simeq 16\,{\rm M}_\odot$ on an eccentric ($e = 0.51 \pm 0.03$) orbit. In addition to having the largest variability amplitude amongst all known heartbeats stars, MACHO 80.7443.1718 is also one of the most massive heartbeat stars yet discovered. The B[e] supergiant has Balmer emission lines and permitted/forbidden metallic emission lines associated with a circumstellar disc. The disc rapidly dissipates at periastron that could indicate mass transfer to the secondary, but re-emerges immediately following periastron passage. MACHO 80.7443.1718 also shows tidally excited oscillations at the $N = 25$ and $N = 41$ orbital harmonics and has a rotational period of 4.4 d.

Key words: binaries: general – stars: early-type – stars: oscillations – stars: massive – stars: variables: general.

1 INTRODUCTION

Heartbeat stars are binaries with short period ($P \lesssim 1$ yr), eccentric ($e \gtrsim 0.3$) orbits. The light curves of heartbeat stars are defined by oscillations outside of periastron combined with a brief, high amplitude ellipsoidal variations at periastron that gives rise to a unique 'heartbeat' signature. Heartbeat stars were first discovered and characterized using data from the *Kepler* space telescope (Borucki et al. 2010; Thompson et al. 2012; Kirk et al. 2016) and its follow-up mission K2 (Howell et al. 2014). *Kepler* identified over 170 heartbeat stars (Kirk et al. 2016). The photometric modulations of these systems are dominated by the effects of tidal distortion, reflection, and Doppler beaming close to periastron (Kumar, Ao & Quataert 1995; Fuller 2017). The variability amplitude of most heartbeat stars is very small (≲1 mmag; Kirk et al. 2016; Hambleton et al. 2018).

Heartbeat stars show tidally excited oscillations (TEOs) at exact integer multiples of the orbital frequency (Fuller 2017) driven by the tidal forcing at periastron. The largest amplitude TEOs are resonances between harmonics of the orbital frequency and the normal mode frequencies of the star (Fuller 2017; Cheng et al. 2020). Most known heartbeat stars are relatively low-mass A and F type stars. However, several massive OB-type heartbeat stars have recently been discovered. For example, ι Ori is a massive heartbeat star system consisting of a O9 III primary and a B1 III-IV companion discovered by BRITE (Pablo et al. 2017) and ϵ Lupi consists of two early-

★ E-mail: jayasinghearachchilage.1@osu.edu
† Resident at Naval Research Laboratory, Washington, DC 20375, USA.

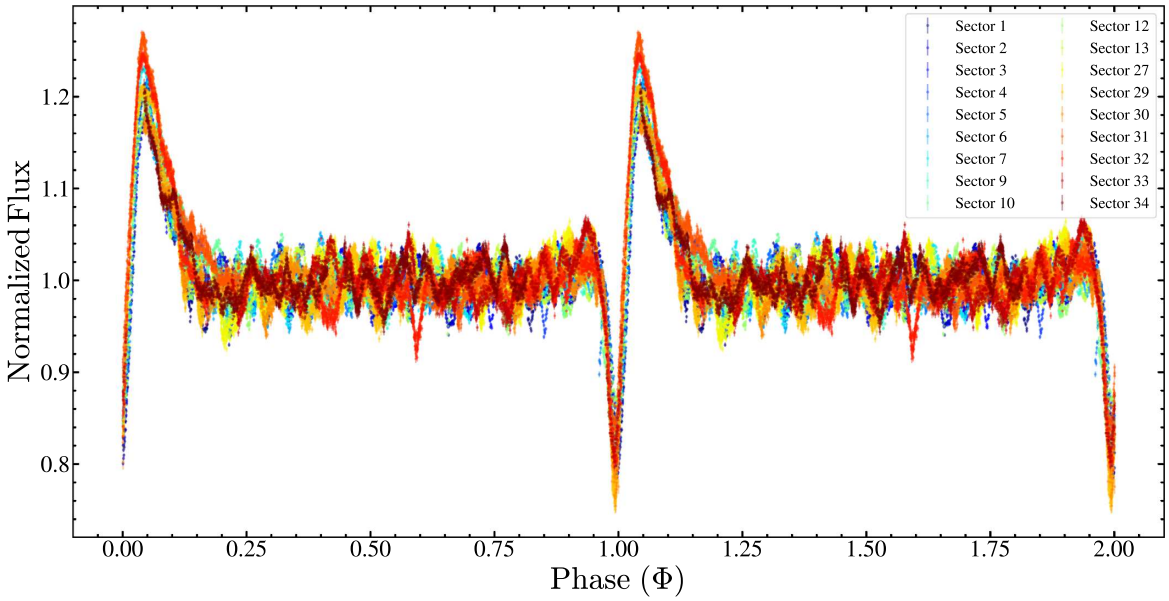

Figure 1. The phased *TESS* light curve for MACHO 80.7443.1718. The points are coloured by the sector.

type main-sequence B stars (Pablo et al. 2019). Recently, Kołaczek-Szymański et al. (2021) identified 20 massive heartbeat stars using data from the Transiting Exoplanet Survey Satellite (*TESS*; Ricker et al. 2015). Heartbeat stars with TEOs are useful laboratories to study equilibrium and dynamical tides (Guo et al. 2020), and massive heartbeat systems can be used to study these processes in the context of binary systems that are the progenitors for compact objects.

MACHO 80.7443.1718 with J2000 coordinates (α, δ) = (81.601924°, −68.784706°), was initially classified as an eclipsing binary in the Large Magellanic Cloud (LMC) with a period of $P \sim$ 32.8 d by the MACHO survey (Alcock et al. 1997). In our previous work (Jayasinghe et al. 2019b), we identified it as a heartbeat star (ASASSN-V J052624.38-684705.6) using data from The All-Sky Automated Survey for SuperNovae (ASAS-SN; Shappee et al. 2014; Kochanek et al. 2017; Jayasinghe et al. 2018, 2019a) and *TESS*. MACHO 80.7443.1718 is a massive star that is part of the LH58 OB association in the LMC, north-west of 30 Doradus. An archival spectrum classified it as a B0.5 Ib/II (Garmany, Massey & Parker 1994), evolved blue star with $U - B = -0.84$ mag, and $B - V = 0.11$ mag (Massey 2002). We found that MACHO 80.7443.1718 displayed the largest known heartbeat flux variations, with a peak-to-peak variability of ∼40 per cent at periastron and oscillation amplitudes of ∼10 per cent due to TEOs outside periastron.

Here, we characterize this extreme amplitude heartbeat star using *TESS* photometry and spectroscopic observations from the Magellan/MIKE and SOAR/Goodman spectrographs. We discuss the *TESS* observations and spectroscopic follow-up in Section 2. In Section 3, we characterize the binary orbit, stellar parameters, and TEOs of this binary system. In Section 4, we discuss the implications of our observations of this unique heartbeat star system. We present a summary of our results in Section 5.

2 OBSERVATIONS

2.1 Photometry

MACHO 80.7443.1718 lies in the Southern *TESS* CVZ which allowed us to extract *TESS* light curves for both Sectors 1 and 2 in Jayasinghe et al. (2019b). Here, we extend the *TESS* photometry using data from sectors 1–7, 9–10, 12–13, 27, and 29–34. We analysed the *TESS* data using an image subtraction pipeline derived from that used to process ASAS-SN data which has been optimized for use with the *TESS* FFIs (Vallely et al. 2020). This pipeline is based on the ISIS package (Alard & Lupton 1998; Alard 2000), and a detailed description of the *TESS*-specific corrective procedures can be found in Vallely et al. (2020).

While this pipeline produces excellent differential flux light curves, the large pixel scale of *TESS* makes it difficult to obtain reliable measurements of the reference flux of a given source. Here, we have estimated the reference flux using the TICGEN software package (Barclay 2017; Stassun et al. 2018). The *TESS*-band magnitude estimates from TICGEN were converted into fluxes using an instrumental zero-point of 20.44 electrons per second in the FFIs, based on the values provided in the TESS Instrument Handbook. Flux was then added to the raw differential light curves such that the median of each sector's observations matched the estimated reference value. This allowed us to produce the normalized flux light curves shown in Fig. 1. The light curves do not include epochs where the observations were compromised by scattered light artefacts from the Earth or Moon.

From the combined *TESS* light curve, we derive an orbital period of

$$P_{\mathrm{orb},TESS} = 32.8194 \pm 0.0105\,\mathrm{d}, \quad (1)$$

which is consistent with the period of

$$P_{\mathrm{orb}} = 32.83627 \pm 0.00846\,\mathrm{d}, \quad (2)$$

derived from the ASAS-SN light curve. For the remainder of this work, we adopt the ASAS-SN orbital period. We use the periastron ephemeris derived from the *TESS* data of

$$\mathrm{BJD}_{\mathrm{periastron}} = 2458373.61518 + 32.83627 \times \mathrm{E}\,, \quad (3)$$

where the epoch E is the number of orbits since the time of minimum. Fig. 1 shows the phased *TESS* light curve for MACHO 80.7443.1718. The strong ellipsoidal variation and TEOs are clearly resolved in the *TESS* data. Following the photometric maximum, we see significant variations in the descending branch of the ellipsoidal variation signal ($0.05 < \Phi < 0.15$). The inclusion of the 16 additional *TESS*

Table 1. Multiband photometry measurements for MACHO 80.7443.1718.

Magnitude	σ	Filter	Reference
14.24	0.04	*UVM*2	This work
14.22	0.03	*UVW*2	This work
13.92	0.04	*UVW*1	This work
12.83	0.10	*U*	Massey (2002)
12.630	0.038	*U*	Zaritsky et al. (2004)
13.67	0.10	*B*	Massey (2002)
13.617	0.106	*B*	Zaritsky et al. (2004)
13.608	0.262	*V*	Zaritsky et al. (2004)
13.56	0.10	*V*	Massey (2002)
13.43	0.10	*R*	Massey (2002)
13.283	0.079	*I*	Zaritsky et al. (2004)
13.255	0.007	*I*	Cioni et al. (2000)
13.020	0.022	*J*	Cutri et al. (2003)
12.978	0.023	*J*	Cioni et al. (2000)
12.833	0.022	*H*	Cutri et al. (2003)
12.734	0.030	K_s	Cutri et al. (2003)
12.411	0.033	[3.6]	Meixner et al. (2006)
12.300	0.030	[4.5]	Meixner et al. (2006)
12.135	0.067	[5.8]	Meixner et al. (2006)
12.416	0.024	*W*1	Wright et al. (2010)
12.337	0.022	*W*2	Wright et al. (2010)
9.901	0.071	*W*3	Wright et al. (2010)
6.197	0.092	*W*4	Wright et al. (2010)

sectors significantly improves our previous analysis of the TEOs (see Section 3.4).

We also retrieve 23 archival photometric measurements spanning 22.2 μm (*W*4) through the *U* band (Table 1). In addition, we obtained archival Swift UVOT (Roming et al. 2005) images in the *UVW*1 (2600 Å), *UVM*2 (2246 Å), and *UVW*2 (1928 Å) bands (Poole et al. 2008) from the LMC Survey (Hagen et al. 2017) pointings 148 and 16. Each epoch of UVOT data includes two observations per filter, which we combined using the UVOTIMSUM package. We then used `uvotsource` to extract source counts using a 6″.0 radius aperture centred on the star. We measured the background counts using a source-free region with radius of ∼18″.0. Using the most recent calibrations (Poole et al. 2008; Breeveld et al. 2010), we converted the UVOT counts into fluxes and magnitudes. We combined all four epochs with a weighted average and summed the uncertainties on the individual epochs with the standard deviation in quadrature to obtain our error estimate. This photometry is used for the spectral energy distribution (SED) models in Section 3.2.

2.2 Optical spectroscopy

We obtained 17 epochs of spectroscopy: 4 with Magellan/MIKE (Bernstein et al. 2003), and 13 with SOAR/Goodman (Clemens, Crain & Anderson 2004), between 2019 January 6 and 2019 August 6. The first and third Magellan Inamori Kyocera Echelle (MIKE) epochs were obtained with a 0″.7 slit, while the other two epochs used a 1″.0 slit. The resolution of the spectra in the region of interest (see below) was about 0.12 and 0.16 Å, respectively, for the two slit widths. Data were obtained for both the blue and red sides of the instrument; here, only data from the blue camera are used. The MIKE data were reduced using CARPY (Kelson et al. 2000; Kelson 2003). The SOAR spectra were taken with a 2100 lines mm^{-1} grating and a 0″.95 slit, giving a resolution of 1.0 Å over the wavelength range ∼4500–5170 Å. The exposure time was 1200 s per epoch. The data were reduced and optimally extracted in the standard manner. For both data sets, we report the mid-exposure observation times as Barycentric Julian Dates (BJD) on the TDB system (Eastman, Siverd & Gaudi 2010). Fig. 2 illustrates the SOAR spectra (excluding two epochs with low signal-to-noise ratio, SNR). We see many emission lines, including the Balmer H β line, suggesting that this source is likely a Be star with a circumstellar disc.

In the majority of the spectra, most of the strong absorption lines are contaminated by emission and hence unusable for radial velocities (RVs). The strongest line without evidence for emission is the He I line at 4922 Å. For the MIKE spectra, we used this absorption line to determine velocities, using a spectrum of the B1 III star HD 68761 from the UVES POP library (Bagnulo et al. 2003) as a template. For the SOAR data, we used the highest SNR SOAR spectrum (that of 2019 March 24) as a template and obtained RVs of the other SOAR spectra through cross-correlation with this template, again in the region of the 4922 Å line. The velocity of the template was determined through cross-correlation with a spectrum of the bright B0 III star HD 114122 taken with the same instrumental set-up. The barycentric RVs of all the spectra are given in Table 2. Note that, due to the rapid rotation of the star and the resulting broad lines, the MIKE spectra do not have substantially smaller velocity uncertainties than the SOAR spectra.

3 RESULTS

3.1 Spectral classification

Using a low-resolution spectrum, MACHO 80.7443.1718 was previously classified as a B0.5 Ib/II star by Garmany et al. (1994). As we previously noted in Section 2, MACHO 80.7443.1718 is an emission-line star with significant continuum emission from a disc that complicates analysis of the spectra. To estimate the spectral type, we calculate the equivalent widths and their ratios in the MIKE spectra for various lines that are typically used to assign spectral types for OB stars (Conti & Alschuler 1971; Mathys 1988; Sota et al. 2011, 2014; Martins 2018). These results are summarized in Table 3.

Based on the classical spectral type criterion for OB stars using the ratio He I 4471/He II 4542, MACHO 80.7443.1718 has a spectral type later than O9.5 (Conti & Alschuler 1971; Mathys 1988). The ratio He I 4144/He II 4200 $= 1.66 \pm 0.50$ is very similar to O9.7 stars with He I 4144/He II 4200 $= 1.98 \pm 1.00$ (Martins 2018). The average ratio of He I 4388/He II 4542 $= 3.37 \pm 0.52$ is somewhat different from O9.7 stars (2.45 ± 0.99) but falls within the reported dispersion in Martins (2018). Based on this analysis, MACHO 80.7443.1718 likely has a spectral type in the range O9.7–B0. Here, we will adopt the B0 spectral type for simplicity.

The luminosity classes of late-O stars can be determined using the ratios Si IV 4089/He I 4026 and He II 4686/He I 4713 which differ significantly for dwarfs and supergiants (Sota et al. 2011, 2014; Martins 2018). Given the uncertainty in our assigned spectral type, we will utilize these criteria to assign a luminosity class even though MACHO 80.7443.1718 was assigned an early B0 spectral type. MACHO 80.7443.1718 has Si IV 4089/He I 4026 $= 1.20 \pm 0.19$ which is most comparable to Ia supergiants that have Si IV 4089/He I 4026 $= 1.07 \pm 0.20$ (Martins 2018). I/Iab stars have Si IV 4089/He I 4026 $= 0.85 \pm 0.11$ (Martins 2018). Similarly, MACHO 80.7443.1718 has He II 4686/He I 4713 $= 0.12 \pm 0.07$ which is again comparable to Ia supergiants with He II 4686/He I 4713 $= 0.31 \pm 0.10$ (Martins 2018). In comparison, I/Iab stars have He II 4686/He I 4713 $= 0.90 \pm 0.30$ (Martins 2018).

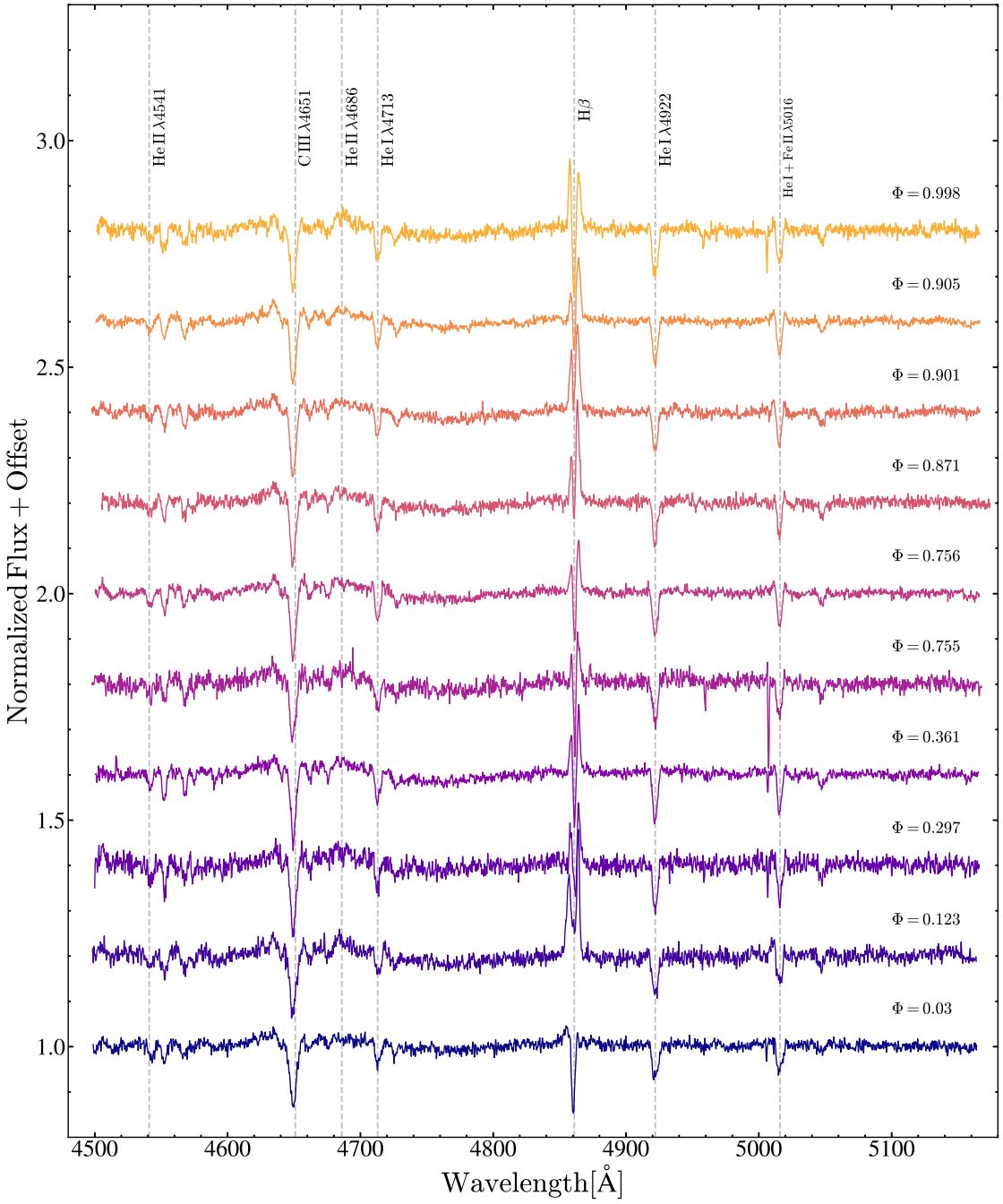

Figure 2. SOAR spectra for MACHO 80.7443.1718 sorted by the orbital phase Φ, where Φ = 0 corresponds to periastron.

Based on this analysis, we assign the B0 Iae spectral type to the primary component of this heartbeat star system. Even though the assignment of a spectral type to this system is complicated by spectral variability, continuum emission from the disc, and the contribution of the companion star, our spectral classification does not differ significantly from that of Garmany et al. (1994).

In Fig. 3, we compare the MIKE spectrum taken on UT 2019-04-06 (Φ = 0.270) with spectra of standard late-O and early-B supergiants. The O-star spectra are obtained from the Galactic O-star catalogue (Maíz Apellániz et al. 2013) and the B-star spectra are obtained from Walborn & Fitzpatrick (1990). While there are differences between the spectra, the assigned B0 spectral type is a reasonable match to the templates.

3.2 Stellar parameters

The absorption lines from the star are broadened, suggesting that it is rapidly rotating. We use the moderate resolution SOAR spectra to measure the projected rotational velocity $v_{\rm rot} \sin i$ in the manner described by Strader et al. (2014) in the region of the 4922 Å line. We convolved the spectrum of the star HD 114122 taken with the same set-up with kernels spanning a range of $v_{\rm rot} \sin i$ and assuming a standard limb darkening law. Cross-correlation of the convolved spectra with the original star yields a relation between the input $v_{\rm rot} \sin i$ and the full width at half-maximum (FWHM) of the cross-correlation peak. Seven of the SOAR spectra had high enough S/N for this measurement, and we found a final value

Table 2. RV measurements for MACHO 80.7443.1718 from SOAR and MIKE.

BJD	Date	Phase (Φ)	RV (kms^{-1})	σ_{RV} (kms^{-1})	Instrument
2458489.6195626	2019-01-06	0.533	271.0	5.8	MIKE
2458498.5758614	2019-01-15	0.806	251.3	5.2	MIKE
2458517.5984611	2019-02-03	0.385	294.7	6.2	MIKE
2458491.6776199	2019-01-08	0.595	254.2	9.8	SOAR
2458525.5646330	2019-02-11	0.627	256.2	12.8	SOAR
2458547.5450865	2019-03-05	0.297	301.2	4.9	SOAR
2458567.4966222	2019-03-24	0.905	245.3	4.0	SOAR
2458579.5027003	2019-04-06	0.270	315.2	6.5	MIKE
2458581.4869998	2019-04-07	0.331	306.8	4.5	SOAR
2458582.4874062	2019-04-08	0.361	294.7	4.8	SOAR
2458595.4763313	2019-04-21	0.756	247.8	4.4	SOAR
2458604.4649556	2019-04-30	0.030	350.9	6.9	SOAR
2458607.5096233	2019-05-04	0.123	360.9	7.3	SOAR
2458664.9182869	2019-06-30	0.871	237.0	6.0	SOAR
2458665.8982865	2019-07-01	0.901	252.8	5.3	SOAR
2458693.9235514	2019-07-29	0.755	251.3	6.4	SOAR
2458701.9156224	2019-08-06	0.998	313.8	5.5	SOAR

Table 3. The average equivalent width ratios and their dispersion calculated using the MIKE spectra.

EW ratio	Measurement
He I λ4471/He II λ4542	5.16 ± 0.71
He I λ4144/He II λ4200	1.66 ± 0.50
He I λ4388/He II λ4542	3.37 ± 0.52
He II λ4686/He I λ4713	0.12 ± 0.07
Si III λ4552/He II λ4542	1.59 ± 0.18
Si IV λ4089/He I λ4026	1.20 ± 0.19

of $v_{\rm rot} \sin i = 174 \pm 34$ km s^{-1}. The uncertainty is the standard deviation of the measurements, which is primarily determined not by the quality of the spectra but by true changes in the shape of the line, perhaps due to a time-variable wind or outflow from the star. Unfortunately, the lack of an appropriate standard star makes it impossible to repeat this analysis for the MIKE spectra. There are indeed variations in the profile of the 4922 Å line in the MIKE spectra, consistent with the findings from the SOAR spectra. From this estimate of $v_{\rm rot} \sin(i)$, the radius from the SED (see below) and the orbital inclination i from Jayasinghe et al. (2019b), the rotational velocity of the primary star is $v_{\rm rot} = 247 \pm 48$ km s^{-1}, which implies a rotation period of $P_{\rm rot} = 4.85 \pm 1.11$ d.

To estimate the surface temperature ($T_{\rm eff}$) and surface gravity ($\log(g)$), we compare the high-resolution MIKE spectra with the TLUSTY OSTAR02 and BSTAR06 model atmospheres at $Z/Z_{\odot} = 0.5$ (Lanz & Hubeny 2003, 2007). The model spectra are convolved using $v \sin i = 174$ km s^{-1}, assuming a standard limb darkening law. We use the BSTAR06 grid for $T_{\rm eff} \leq 30\,000$ K and the OSTAR02 grid for $T_{\rm eff} > 30\,000$ K. The BSTAR06 grid extends to $T_{\rm eff} = 30\,000$ K with a grid spacing of $\Delta T_{\rm eff} = 1000$ K and $\Delta \log(g) = 0.25$. In comparison, the OSTAR02 grid begins at $T_{\rm eff} = 27\,500$ K with a grid spacing of $\Delta T_{\rm eff} = 2500$ K and $\Delta \log(g) = 0.25$.

To determine $T_{\rm eff}$ and $\log(g)$, the MIKE spectra are compared with the model atmospheres at various He I and He II absorption lines. The best overall fit is returned for a model atmosphere with $T_{\rm eff} = 30\,000$ K and $\log(g) = 3.25$. Fig. 4 compares the model atmospheres at a fixed surface gravity of $\log(g) = 3.25$ but with various temperatures against the MIKE spectrum at $\Phi = 0.806$ for the He lines He I λ4922 and He II λ4200. We use these lines because they are less affected by emission from the disc. He II is particularly sensitive to the surface temperature and the observed He II λ4200 line best agrees with $T_{\rm eff} = 30\,000$ K. Higher surface temperatures are clearly incompatible with our observations.

Fig. 5 compares the best model atmosphere with $T_{\rm eff} = 30\,000$ K and $\log(g) = 3.25$ to the MIKE spectra of selected He I and He II absorption lines. There is clear evidence for spectral variability and emission components in the He I lines, particularly the emission component is distinctly seen in the He I λ4471 line. The He II λ4541 and He II λ4686 lines are relatively weak compared to the He II λ4200 line. However, the equivalent width of the He II λ4686 line grows weaker with increasing luminosity, and is weakest for the Ia luminosity class (Martins 2018). This is entirely consistent with the B0 Iae spectral type that we assigned previously (see Section 3.1).

Using the *UBV* photometry in Table 1, we can derive a photometric temperature using the classical reddening free Q parameter (Johnson 1958; Bragança et al. 2012), defined as $Q = (U - B) - X(B - V)$, with $X = E(U - B)/E(B - V)$. The Q parameter can then be used to estimate the temperature using the calibration given by Massey et al. (1989)

$$\log(T_{\rm eff}) = 3.944 - 0.267Q + 0.364Q^2. \quad (4)$$

Using a standard value ($X = 0.72$) for the reddening ratio, we obtain $Q = -0.9791$, which implies $\log(T_{\rm eff}) = 4.554$ and $T_{\rm eff} \simeq 36\,000$ K. Using a similar method, Massey (2002) estimated a higher temperature of $T_{\rm eff} \simeq 39\,000$ K for this source. These photometric estimates of the temperature are considerably higher than our spectroscopic estimate but they are less reliable. The lack of strong He II absorption lines in the spectra also rule out this higher temperature estimate.

We used DUSTY (Ivezic & Elitzur 1997; Elitzur & Ivezić 2001) inside a Markov chain Monte Carlo (MCMC) wrapper (Adams & Kochanek 2015) to fit the SED of MACHO 80.7443.1718 using the 18 photometric measurements spanning 3.6 μm through the *UVM2* band (Table 1). We assumed foreground extinction due to $R_V = 3.1$ dust (Cardelli, Clayton & Mathis 1989) and used Castelli & Kurucz (2003) model atmospheres for the star. Since MACHO 80.7443.1718 is located in the LMC, we assume a distance of $d_{\rm LMC} = 50$ kpc (Pietrzyński et al. 2013). Assuming minimum luminosity uncertainties of 10 per cent for each band, the fits have $\chi^2/N_{\rm dof} \simeq 1$ at fixed $T_{\rm eff}$. Fig. 6 shows the SED for MACHO 80.7443.1718. While these models are adequate for determining the luminosity and extinction at fixed temperature, they are not reliable

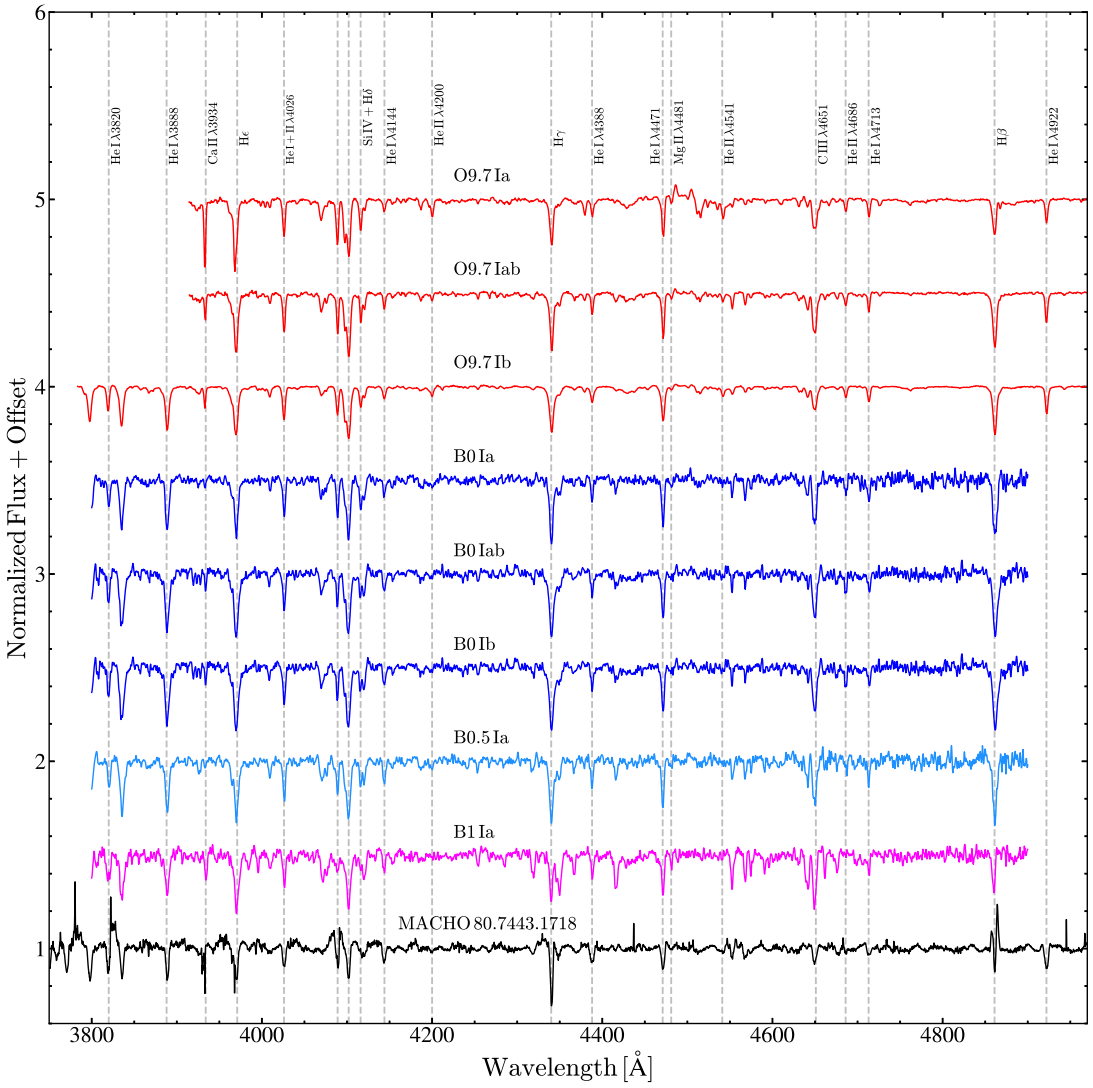

Figure 3. Comparison of various spectral type standards from Maíz Apellániz et al. (2013) and Walborn & Fitzpatrick (1990) with the MIKE spectrum at phase $\Phi = 0.270$ (black).

for determining a temperature (especially since they all lie on the Rayleigh–Jeans side of the SED). For $T_{\rm eff} \simeq 30\,000$ K, we obtain $\log(L/L_\odot) = 5.61 \pm 0.04$ with $E(B-V) \simeq 0.39 \pm 0.02$ mag.

With the luminosity and temperature constrained, we can estimate the mass of the primary star using MIST stellar evolutionary tracks (Choi et al. 2016; Dotter 2016) computed with the Modules for Experiments in Stellar Astrophysics code (MESA; Paxton et al. 2011, 2013, 2015). We use tracks for stars with a metallicity of [Fe/H] = −0.4, which is the average metallicity of the LMC (Choudhury, Subramaniam & Cole 2016). The position of MACHO 80.7443.1718 in the Hertzsprung–Russell diagram (HRD) (Fig. 7) is consistent with a primary star of mass $M_1 = 34.5^{+1.5}_{-2.0}\,{\rm M}_\odot$ starting to evolve across the Hertzsprung gap. In the MIST tracks, a $34.5\,{\rm M}_\odot$ star with $T_{\rm eff} \simeq 30,000$ K and $\log(L/L_\odot) \simeq 5.6$ has $\log(g) = 3.2$ which is consistent with the spectroscopic estimate of $\log(g) = 3.25 \pm 0.25$. Given the luminosity and the temperature, the radius of the primary is $R_1 = 23.7^{+2.9}_{-1.2}\,{\rm R}_\odot$. For these estimates of the mass and radius, the break-up velocity of the star is $\sim$530 km s^{-1}. This implies that MACHO 80.7443.1718 is rotating at $\Omega/\Omega_{\rm crit} \sim 0.47$.

At its current evolutionary state in the MIST tracks, the age of the primary star is ∼5.8 Myr. Assuming that MACHO 80.7443.1718 is coeval with the LH58 OB association, we can verify its age by fitting isochrones to the LH58 colour–magnitude diagram (CMD) using the photometry from Garmany et al. (1994). We estimate the global extinction towards LH58 by varying $E(B-V)$ to minimize the residuals between main-sequence stars and a 1 Myr MIST isochrone with [Fe/H] = −0.4. We do not consider differential extinction to the members of this association. With this we obtain a reddening of $E(B-V) = 0.17 \pm 0.01$ mag which we then use to deredden the LH58 photometry. The reddening towards MACHO 80.7443.1718 ($E(B-V) \simeq 0.39 \pm 0.02$ mag) is larger than the reddening towards the LH58 association by $\Delta E(B-V) \sim 0.22$ mag, suggesting the presence of circumstellar dust consistent with the estimated age of the star. Fig. 8 shows the dereddened CMD for the LH58 OB association. The CMD is best-fitted by an isochrone at ∼5.6 Myr, which is consistent with the age estimate of the primary from the MIST models (Fig. 7). We estimate the age of the LH58 association, and hence the age of MACHO 80.7443.1718 as $5.6^{+1.5}_{-1.1}$ Myr.

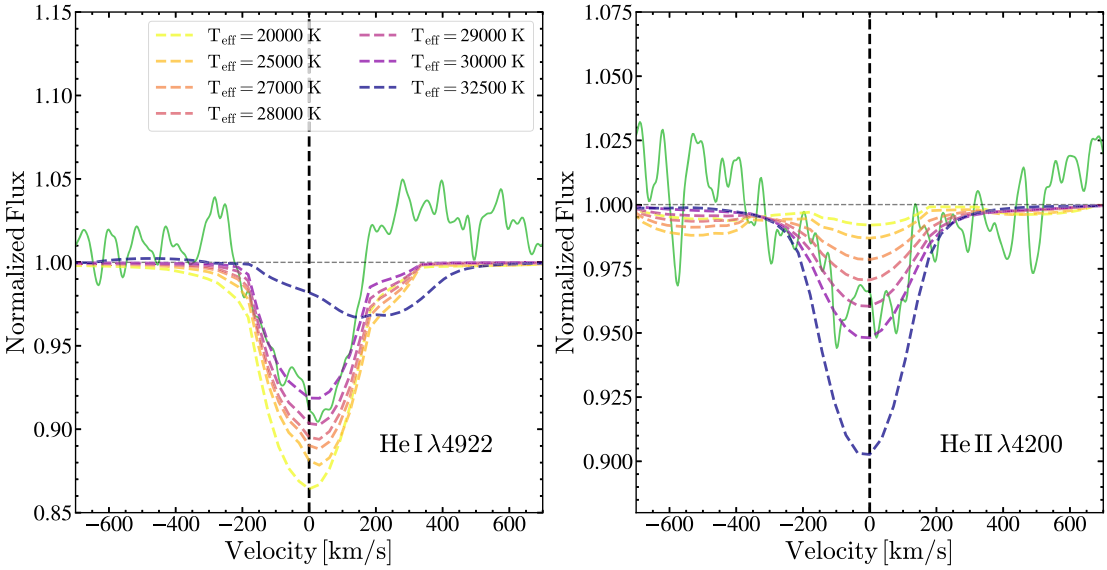

Figure 4. Comparison of various BSTARO6 and OSTAR02 model atmospheres (Lanz & Hubeny 2003, 2007) at a fixed surface gravity of $\log(g) = 3.25$ (dashed lines) against the MIKE spectrum at $\Phi = 0.806$ for the He I λ4922 and He II λ4200 absorption lines. The MIKE spectrum has been smoothed using a Gaussian kernel but not by enough to modify the line profiles.

3.3 Binary solution

Previously, we used the analytical model from Kumar et al. (1995, their equation 44) to model the flux variations produced by the tidal distortions at periastron (Jayasinghe et al. 2019b). This model has been used to fit the light curves of other heartbeat stars (Thompson et al. 2012). The fit returns the true anomaly, $\phi(t)$, the angle of periastron, ω, the orbital inclination, i, and the eccentricity, e, as parameters. We attempted fitting a standard eclipsing binary model including irradiation and reflection effects using PHOEBE 2.3 (Prša et al. 2016; Horvat et al. 2018) but were unable to replicate the observed variability amplitude. To accurately model the photometric variability of this unique system, the circumstellar disc will also need to be considered in addition to modelling the dynamical tidal interactions and the two stellar components. We refit the combined *TESS* light curve with the Kumar et al. (1995) analytical model using the MCMC sampler EMCEE (Foreman-Mackey et al. 2013). We obtain results that are consistent with our previous model (see Jayasinghe et al. 2019b) with $i = 43.9° \pm 0.2°$, $e = 0.565 \pm 0.002$, and $\omega = 298.2° \pm 1.0°$. Hereafter, we will use the orbital inclination from the updated fit.

We fit eccentric Keplerian models to the RVs using the custom Monte Carlo sampler THEJOKER (Price-Whelan et al. 2017). Since the time span of the RVs is much shorter than the photometry, the orbital period is not left as a free parameter. Instead, we use a prior to constrain the period by the photometric estimate in equation (2) ($P = 32.8363 \pm 0.0085$ d). Leaving the rest of the parameters free, we find a BJD time of periastron $T_P = 2458505.595 \pm 0.301$ d, eccentricity $e = 0.506 \pm 0.033$, argument of periastron $\omega = 302.1 \pm 5.1°$, semi-amplitude $K_1 = 62.9 \pm 4.0$ km s^{-1}, and systemic velocity $\gamma = 289.6 \pm 1.5$ km s^{-1}. There are no significant correlations between the variables except for the expected correlation between T_P and ω. This fit has a $\chi^2 = 10.0$ for 12 d.o.f. and an rms residual of 4.6 km s^{-1}, and so is a good fit to the data.

Fitting the *TESS* photometry gives an independent estimate of T_P (Jayasinghe et al. 2019b). This *TESS* value, extrapolated with the appropriate uncertainty to the first value within the time range of our velocities, is $T_P = 2458505.470 \pm 0.034$ d. This is entirely consistent with the RV-only measurement of T_P, but more precise. If we refit the eccentric model with this estimate as a constraint, the values are very similar: $e = 0.507 \pm 0.033$, $\omega = 300.2 \pm 2.0°$, $K_1 = 61.9 \pm 2.8$ km s^{-1}, and $\gamma = 289.4 \pm 1.5$ km s^{-1}. The goodness of fit is nearly identical at $\chi^2 = 10.3$ for 13 d.o.f. and an rms of 4.7 km s^{-1}. This fit is shown in Fig. 9. We adopt these parameters as our final spectroscopic model. The value for ω derived from the radial velocities is entirely consistent with the photometric estimate to $<1\sigma$. The eccentricity derived from the radial velocities is slightly smaller ($\sim 1.8\sigma$) than that obtained from the fit to the light curve.

Using the posterior samples, the binary mass function is

$$f(M) = \frac{P_{\rm orb} K_1^3 (1 - {\rm e}^2)^{3/2}}{(2\pi G)} = 0.51^{+0.07}_{-0.06}\,{\rm M}_\odot \quad (5)$$

Using this value of $f(M)$, $M_1 = 34.5^{+1.5}_{-2.0}\,{\rm M}_\odot$, and an inclination angle $i = 43.9 \pm 0.2°$ from the heartbeat model, we find that the mass of the secondary is $M_2 = 15.7 \pm 1.3\,{\rm M}_\odot$. Fig. 10 illustrates the mass of the companion as a function of the mass of the primary. Even for an edge-on orbit, the minimum mass of the companion is $M_2 \simeq 10\,{\rm M}_\odot$. The primary is well within its Roche radius ($R_{\rm L} \simeq 71\,R_\odot \simeq 3.0\,R_*$), but at periastron, it approaches Roche lobe overflow with a fillout factor $f = R_*/R_{L,\,\rm peri} \simeq 0.7$. We do not see strong evidence for a secondary star in our spectra.

To obtain estimates of the stellar parameters of the secondary star, we use the MIST single-star models assuming that the secondary is coeval with the primary. While these models do not account for binary interactions, they can provide a useful estimate of the properties of the unseen secondary star. The MIST models suggest that the secondary star has a similar temperature to the primary, with $T_{\rm eff} \sim 31\,600$ K. Unlike the primary, the secondary star should be on the main sequence with $\log(g) = 4.1 \pm 0.1$. The MIST models indicate that the secondary has ~7 per cent of the primary's luminosity. Given that the secondary has a similar effective temperature and a considerably lower luminosity than the primary, it is challenging to recover the properties of the secondary star from the spectra. Using the calibrations from Martins, Schaerer & Hillier (2005) for main-sequence stars, the secondary star should have an O9.5 spectral type.

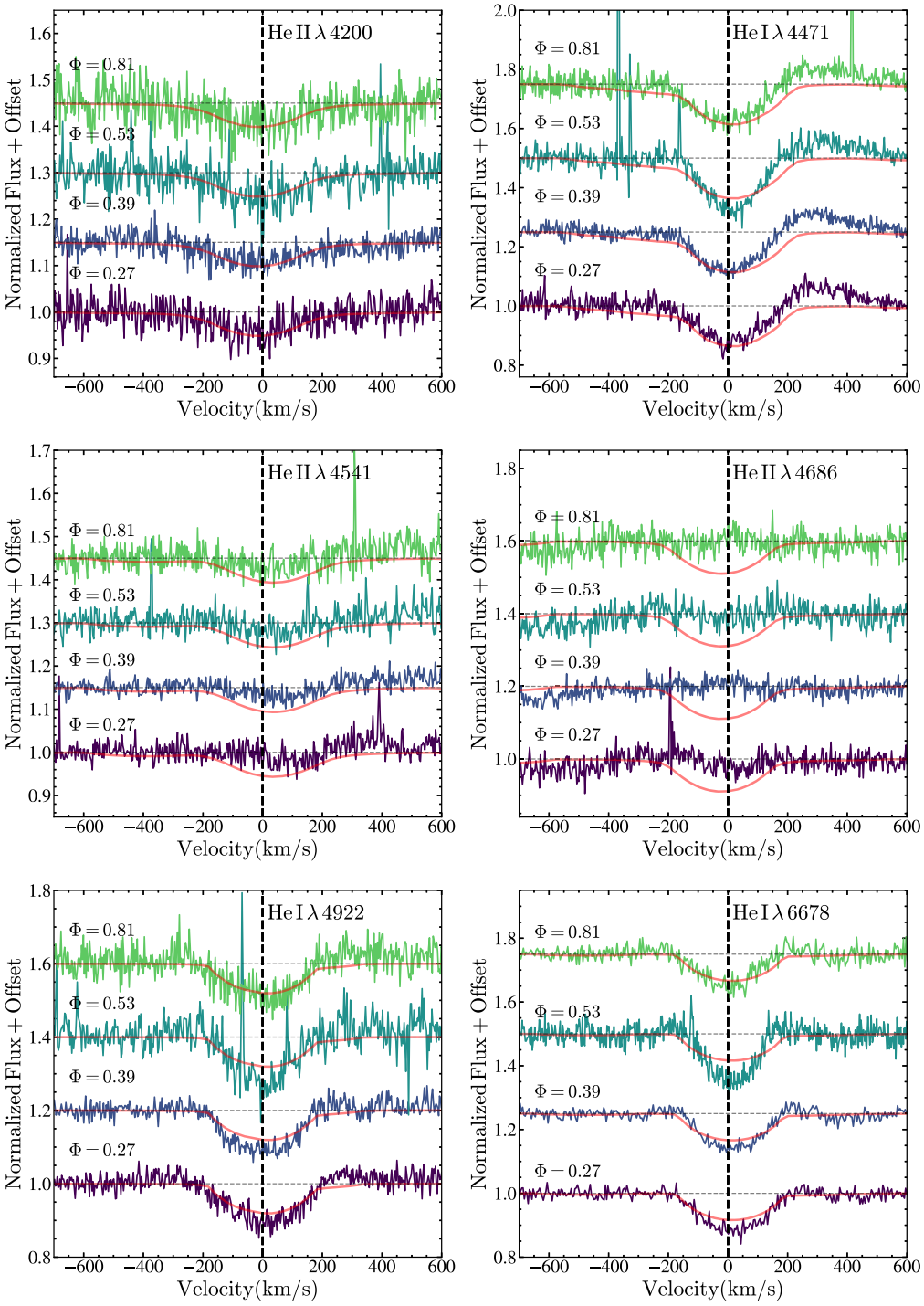

Figure 5. MIKE line profiles for He II λ4200, He I λ4471, He II λ4541, He II λ4686, He I λ4922, and He I λ6678. The TLUSTY BSTAR06 model atmosphere with $T_{\rm eff}$ = 30 000 K and log (g) = 3.25 is shown in red (Lanz & Hubeny 2003, 2007).

We will adopt this spectral type and the stellar properties from the MIST models for the secondary. The binary and stellar properties for MACHO 80.7443.1718 are summarized in Table 4.

3.4 Tidally excited oscillations

Previously, we analysed both the ASAS-SN and *TESS* light curves for TEOs. In both the ASAS-SN and *TESS* data, we identified a TEO corresponding to the N = 25 orbital harmonic (Jayasinghe et al. 2019b). We also recovered a possible TEO at N = 8 and N = 7 in the ASAS-SN and TESS data, respectively. However, due to the limited baseline of the *TESS* data (two sectors) in our previous work, the resolution of the peaks in the Fast Fourier Transform (FFT) spectrum was poor. Here, we use all 18 sectors of *TESS* data to analyse the FFT power spectrum for MACHO 80.7443.1718.

We search for TEOs in the *TESS* data using only the orbital phases 0.25 ≤ Φ ≤ 0.85 by calculating the FFT using the PERIOD04 software package (Lenz & Breger 2005). We iteratively whitened the

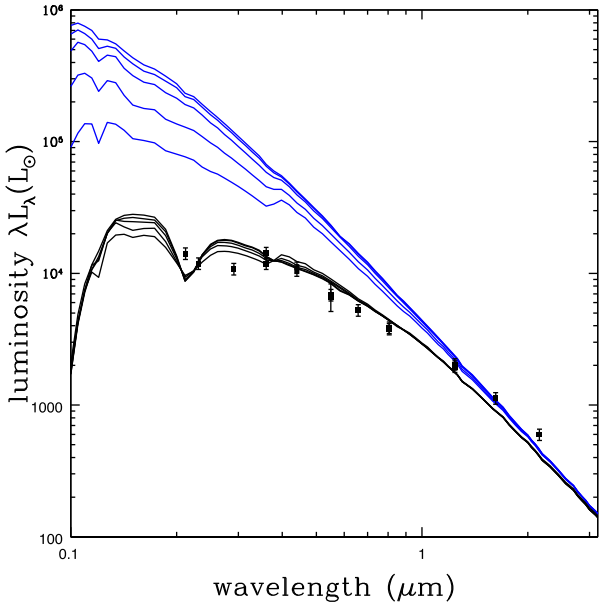

Figure 6. The SED for MACHO 80.7443.1718. The blue lines show the actual stellar SEDs at various $T_{\rm eff}$, and the black lines show these SEDs with reddening.

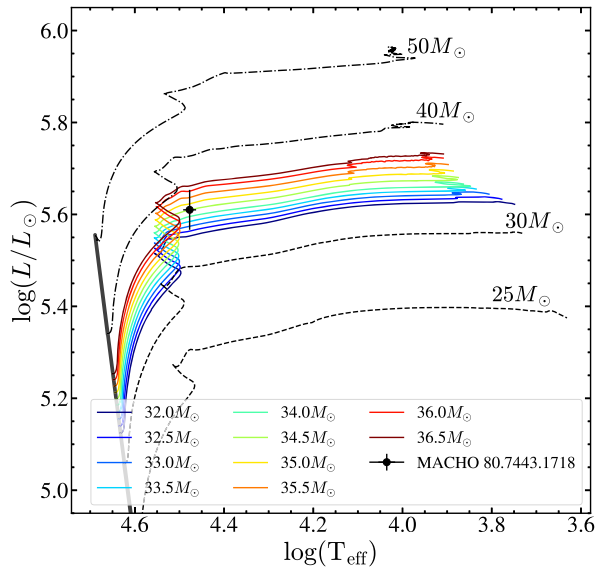

Figure 7. The HRD for MACHO 80.7443.1718. MIST evolutionary tracks (Choi et al. 2016; Dotter 2016) are shown for stars at various masses with a metallicity of [Fe/H] = −0.4.

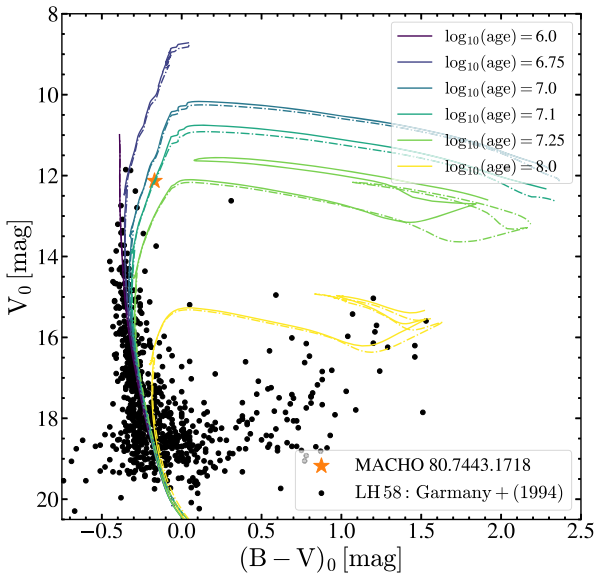

Figure 8. The dereddened CMD for the LH58 OB association. MIST isochrones (Choi et al. 2016; Dotter 2016) are shown for populations with a metallicity of [Fe/H] = −0.4.

light curves by fitting sinusoids using the dominant frequency. Peaks with SNR >3 were retained. Table 5 lists the frequencies that were retrieved from this analysis of the *TESS* data. The frequencies were optimized to reduce the light-curve residuals and the uncertainties were determined using a Monte Carlo analysis within PERIOD04. The TEO at the $N = 25$ mode was the dominant frequency ($P = 1.312$ d) with SNR = 8.2. Fig. 11 illustrates the FFT power spectrum before and after subtracting the dominant TEO at $N = 25$. Modes corresponding to the $N = 22$, 23, 24, 26, and 27 orbital harmonics are also seen in the power spectrum prior to the subtraction of the TEO at $N = 25$ but are not significant after the light curve is whitened.

We identify two other modes in the FFT analysis at $P = 4.438$ d and $P = 0.800$ d. The latter mode corresponds to a TEO at the $N = 41$ orbital harmonic, however, the peak at $P = 4.438$ d is significantly (∼40 per cent) different from the nearest orbital harmonic. A similar frequency was also recovered from the ASAS-SN and TESS data in Jayasinghe et al. (2019b) with $P = 4.148$ d and $P = 4.621$ d, which we previously attributed to a TEO. However, this mode is very similar to the predicted orbital period of the primary star ($P_{\rm rot} = 4.85 \pm 1.11$ d) that we estimated from the measurement of $v_{\rm rot} \sin i$ in Section 3.2, and is unlikely to be a TEO given its significant deviation from the nearest TEO. This period implies that $v_{\rm rot} \sin i = 188 \pm 23$ km s^{-1} assuming the radius from the SED fit (Section 3.2) and the orbital inclination from the heartbeat model (Section 3.3), which is consistent with the spectroscopic estimate ($v_{\rm rot} \sin i = 174 \pm 34$ km s^{-1}). Studies of the photometric variability in Be stars have noted that periodic variability longward of 2 d could correspond to the beating of non-radial pulsation modes, stellar rotation, Rossby modes, or circumstellar activity (Sterken, Vogt & Mennickent 1996; Labadie-Bartz et al. 2017). The position of MACHO 80.7443.1718 in the HRD (Fig. 7), and the period at $P = 4.438$ d rules out pulsations (Miglio, Montalbán & Dupret 2007). Given that this mode is within ∼8 per cent of the expected rotational period of the primary, we believe that this signal originates due to the rotation of the star.

We attempt to identify the pulsation modes corresponding to the $N = 25$ and $N = 41$ TEOs using tidal theory and models of stellar structure (see e.g. Fuller 2017; Cheng et al. 2020; Guo et al. 2020). Assuming that the TEOs are adiabatic and are standing waves that are not fine-tuned, Guo et al. (2020) approximate the pulsation phases for the dominant $l = 2$ modes in heartbeat stars as

$$\phi_{l=2,m} = \begin{cases} 0.25 + m\phi_0 & \text{if } m = 2 \text{ or } -2 \\ 0.25 & \text{if } m = 0 \end{cases} \quad (6)$$

where $\phi_0 = 0.25 - \omega/2\pi$ is the observer's longitudinal coordinate and m is the mode azimuthal number. These phases are defined with respect to the time of periastron ($\phi = 0$). In the case of MACHO 80.7443.1718, $\phi_0 \simeq -0.58$. The retrograde ($m = 2$) or prograde ($m = -2$) modes have a 180° phase ambiguity, thus a 0.5 phase offset

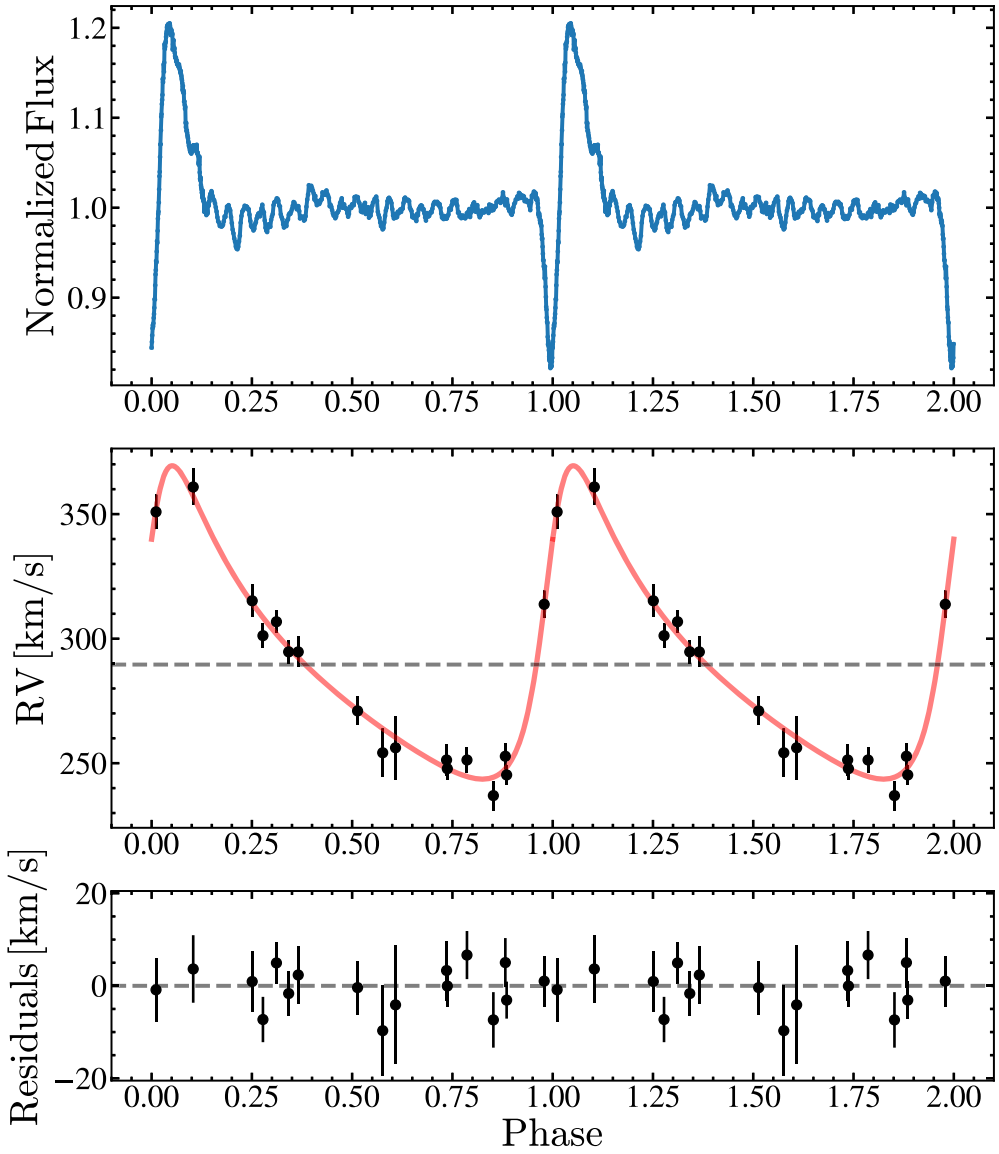

Figure 9. The best-fitting Keplerian model to the RV data (red line) for MACHO 80.7443.1718 (middle) compared to the averaged *TESS* light curve (top). The bottom panel shows the velocity residuals.

can be added or subtracted from equation (6). Therefore, the $m = |2|$ modes can have $\phi \simeq 0.41$ or $\phi \simeq 0.92$. For the $N = 25$ TEO we found $\phi \simeq 0.25$, which is entirely consistent with the $m = 0$ mode ($\phi = 0.25$). The $N = 41$ TEO has $\phi \simeq 0.97$, which is consistent with the $m = |2|$ mode. The phase deviation for the $N = 41$ TEO $\Delta\phi(m = |2|) \simeq 0.05$ can occur due to the non-adiabicity of the pulsations and spin–orbit misalignments (Guo et al. 2020).

We also attempted to track the changes in amplitude and phase for the three frequencies in Table 5 across the periastron passages in the *TESS* data. Once it became clear that simple models of the oscillations would not work, we did not pursue this further. It would be interesting, however, to look for variations in the individual modes across periastron passages.

3.5 The B[e] phenomenon

The presence of emission lines in both the SOAR and MIKE spectra suggest that MACHO 80.7443.1718 contains a circumstellar disc. This phenomenon is commonly associated with the classical Be stars (Rivinius, Carciofi & Martayan 2013). Classical Be stars are rapidly rotating main-sequence B stars that form a Keplerian 'decretion' disc (Rivinius et al. 2013). However, this phenomenon also extends to supergiants like MACHO 80.7443.1718 (Kraus 2019). B[e] supergiants have early B spectral types and show strong Balmer emission alongside narrow emission lines from both permitted and forbidden transitions (Kraus, Borges Fernandes & de Araújo 2010; Kraus 2019). B[e] supergiants (hereafter B[e] SGs) in the Magellanic Clouds typically have luminosities in the range $\log(L/L_{\odot}) \sim 4.0$–$6.0$ and have excesses in the near-infrared (NIR) caused by hot $\sim$1000 K dust (Lamers et al. 1998; Zickgraf 2006). B[e] SG winds have a hot, fast line-driven polar component alongside a cool, slow, equatorial component from which forbidden emission lines (for e.g. [O I] and [Fe II] lines) originate (Lamers et al. 1998; Zickgraf 2006; Kraus 2019).

The Balmer line profiles of MACHO 80.7443.1718 show evidence of disc formation and disruption coinciding with the binary orbit.

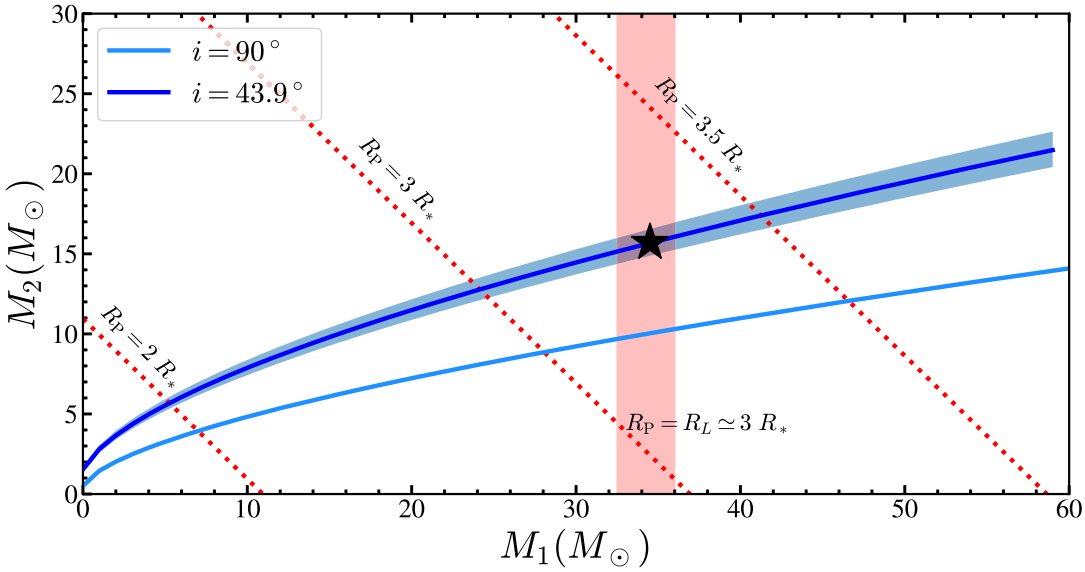

Figure 10. The mass of the companion (M_2) as a function of the mass of the primary (M_1). The binary mass function at inclinations of $i = 90°$ and 43.9° are shown as the solid lines. Where the periastron distances would correspond to $R_P = 2\ R_*$, $3\ R_*$, $3.5\ R_*$ and the Roche radius ($R_L \simeq 3\ R_*$) are shown by the dotted lines. The derived values for M_1 and M_2 are illustrated as the black star and the uncertainty in the mass of the primary star and the binary mass function are shaded.

Table 4. Fundamental parameters for MACHO 80.7443.1718.

Parameter	Primary	Secondary	Reference
$P_{\rm orb}$ (d)	32.83627 ± 0.00846		Jayasinghe et al. (2019b)
T_P(HJD − 2450000)	8505.470 ± 0.034		Jayasinghe et al. (2019b)
i (°)	43.9 ± 0.2		This work
ω (°)	300.2 ± 2.0		This work
e	0.507 ± 0.033		This work
γ (kms^{-1})	289.4 ± 1.5		This work
K (kms^{-1})	61.9 ± 2.8	–	This work
$f(M)$ (M$_\odot$)	$0.51^{+0.07}_{-0.06}$		This work
$v\ \sin(i)$ (kms^{-1})	174 ± 34	–	This work
$T_{\rm eff}$ (K)	$30\,000 \pm 1000$	$31\,600 \pm 1000$	This work
log ($L/L_\odot$)	5.61 ± 0.04	$4.46^{+0.11}_{-0.12}$	This work
log (g)	3.25 ± 0.25	4.1 ± 0.1	This work
R ($R_\odot$)	$23.7^{+2.9}_{-1.2} R_\odot$	$5.7^{+0.4}_{-0.5} R_\odot$	This work
M (M$_\odot$)	$34.5^{+1.5}_{-2.0}$ M$_\odot$	15.7 ± 1.3	This work
[Fe/H]	−0.4 (Fixed)		This work
Spectral type	B0 Iae	O9.5 V	This work
Age (Myr)	$5.6^{+1.5}_{-1.1}$		This work
$E(B-V)$ (mag)	0.39 ± 0.02		This work

Table 5. Frequencies for MACHO 80.7443.1718, phased to periastron calculated using the multisector *TESS* light curve. The errors in frequency, amplitude, and phase are calculated through a Monte Carlo analysis.

Type	Frequency ν (d^{-1})	Orbital harmonic N	$\nu/N\nu_{\rm orb}$	Amplitude (ppt)	Phase	SNR
TEOs						
	0.76207 ± 0.00001	25	1.0009	8.4 ± 0.2	0.251 ± 0.003	8.2
	1.24944 ± 0.00004	41	1.0007	2.0 ± 0.2	0.969 ± 0.014	3.3
Rotation						
	0.22530 ± 0.00119	–	–	4.4 ± 0.8	0.254 ± 0.069	3.5

Fig. 12 shows the Hβ line profiles in the SOAR spectra as a function of orbital phase. The typical Gaussian FWHM of the Hβ line is ∼675 km s^{-1}. Hβ emission is typically produced close to the star, at a few R_* (Negueruela et al. 2000). Close to periastron (Φ = 0.030), we see little evidence of a disc, with Hβ in absorption and very little emission. In the span of ∼4 d ($\Phi = 0.123$), the Hβ line profile evolves into a double-peaked line profile. Be outbursts occur due to mass outflows from the stellar surface to the circumstellar

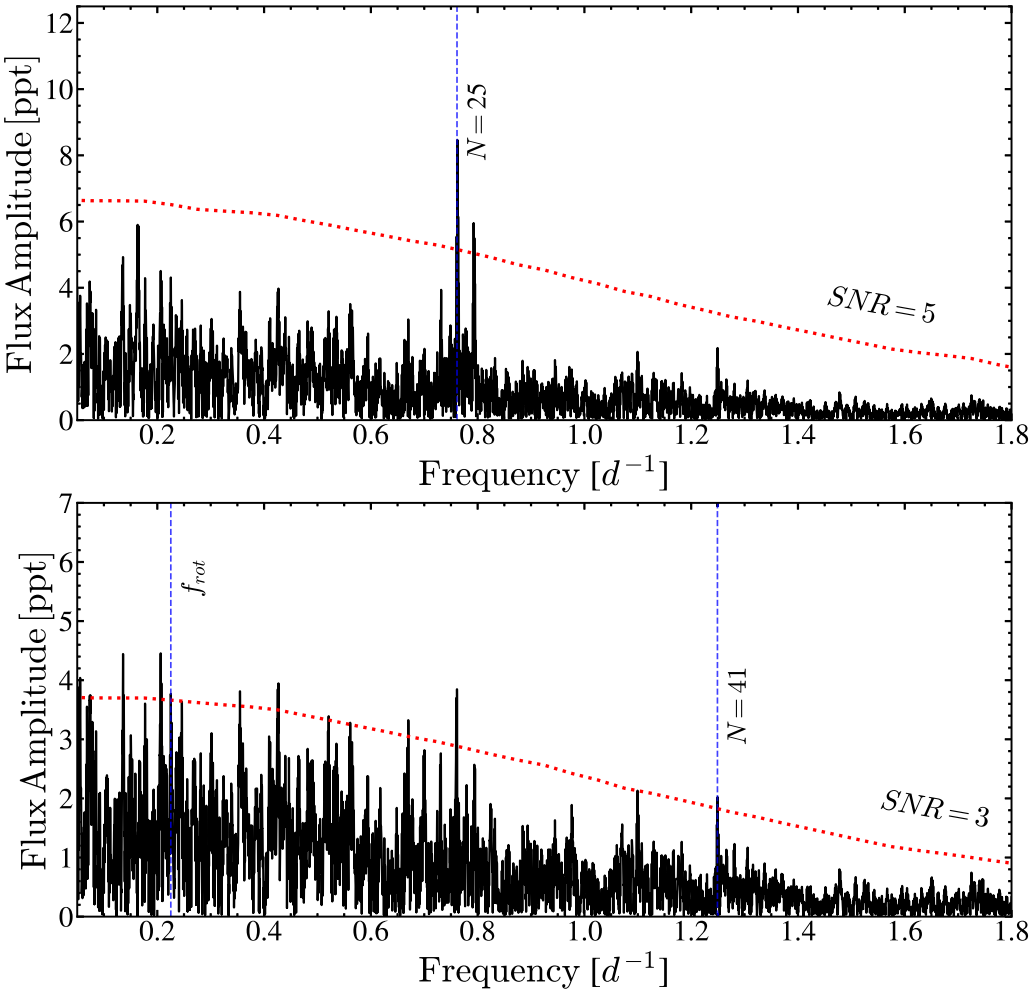

Figure 11. FFT power spectrum of the combined *TESS* light curve before (top) and after (bottom) subtracting the dominant TEO at $N = 25$. The red dashed lines show the flux amplitudes at which SNR = 5 (top) and SNR = 3 (bottom) as a function of frequency. The frequencies identified in our analysis are shown in blue.

disc (Labadie-Bartz et al. 2017). At the intermediate orbital phases where TEOs dominate ($0.25 \leq \Phi \leq 0.85$), the Hβ line profile shows deep shell absorption with emission wings. At late phases, before periastron passage ($\Phi > 0.85$), the shell-like line profile evolves to show emission, although the emission is weaker than that seen right after periastron.

The violet-to-red (*V*/*R*) ratio of the double-peaked emission lines is a useful quantity to study Be star emission lines (Mennickent & Vogt 1991). The violet (*V*) peak dominates when material approaches the observer whereas the red (*R*) peak dominates when material moves away from the observer. Variations in the *V*/*R* ratio are related to the dynamics of the cirumstellar disc which include global disc oscillations (Labadie-Bartz et al. 2017). Fig. 13 shows the evolution of the *V*/*R* ratio and the equivalent widths (EW(Hβ)) of the Hβ line profiles with the orbital phase. This system shows significant *V*/*R* variability. At periastron, the Hβ symmetry is $V > R$, which immediately reverses to $V < R$ within $\Delta\Phi \sim 0.2$. The equivalent width appears to be correlated with the orbital phase, and suggests that the system undergoes significant outbursts immediately before ($\Phi \sim 0.9$) and after ($\Phi \sim 0.1$) approaching periastron. At the intermediate orbital phases ($0.25 \leq \Phi \leq 0.85$), the equivalent widths are mostly similar.

Fig. 14 shows the *TESS* photometry and the SOAR Hβ line profiles at $\Phi = 0.030$ and $\Phi = 0.123$ corresponding to periastron passage and the first spectroscopic epoch with evidence of a circumstellar disc, respectively. When compared to a model of the tidal distortions at periastron (Kumar et al. 1995), the *TESS* light curve shows photometric evidence of outbursts occurring immediately following periastron while the star is tidally deformed. In fact, the scatter in the *TESS* light curve beyond $\Phi \sim 0.05$ suggests that the circumstellar disc might form earlier than $\Phi = 0.123$. The TEOs following periastron passage likely contribute to mass-loss and disc formation.

Fig. 15 shows the Balmer line profiles in the high-resolution MIKE spectra as a function of orbital phase. There is clear evidence for strong Hα emission. Previous studies of Be stars have shown that Hα emission probes a region up to $\sim 10 R_*$ (Hummel & Vrancken 1995; Quirrenbach et al. 1997). The Gaussian FWHM of the Hα line is $\sim 620\,\mathrm{km\,s^{-1}}$ and its equivalent width EW(Hα) varies from $\sim$14 to 26 Å. The Hα line profile is complex, with numerous sharp absorption/emission components that vary with orbital phase. The MIKE Hβ line profiles are comparable to those obtained from SOAR and show shell absorption alongside emission wings at intermediary orbital phases.

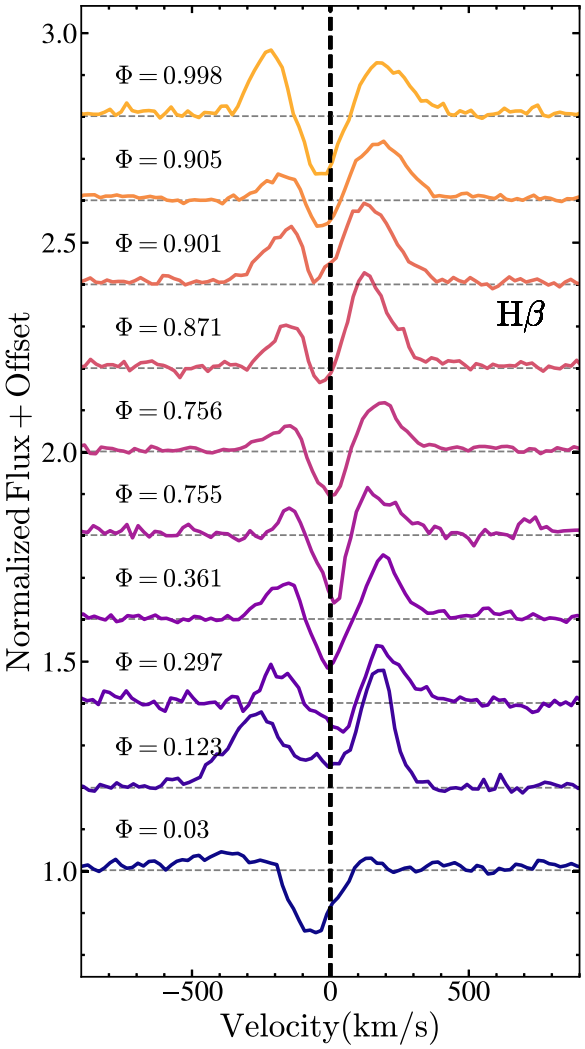

Figure 12. SOAR Hβ line profiles for MACHO 80.7443.1718 sorted by orbital phase.

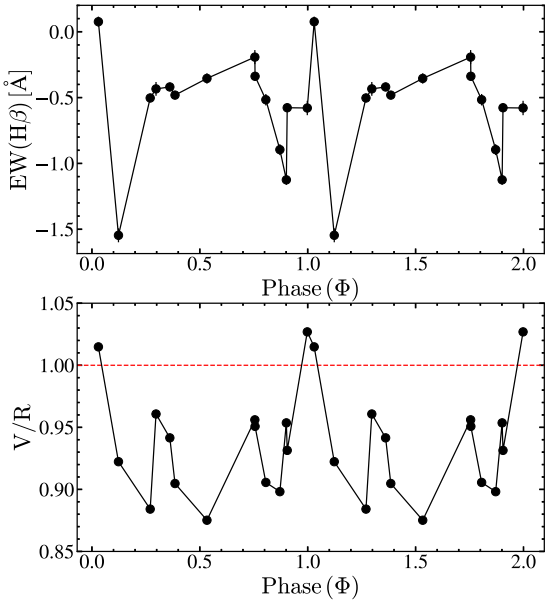

Figure 13. The equivalent width of the Hβ line (top) and the V/R ratio (bottom) as a function of orbital phase Φ.

To confirm the B[e] classification, we search for the presence of forbidden emission lines in the high-resolution MIKE spectra, focusing on the [O I] and [Fe II] lines (Fig. 16). Forbidden emission lines are optically thin and collisionally excited. We do not see evidence for [O I] emission lines in the two MIKE spectra at Φ = 0.270 and Φ = 0.385. We note the presence of the [O I] λ6300 line (single-peaked) at Φ = 0.533 but not at Φ = 0.806. Compared to the radial velocity of the primary, the [O I] λ6300 line has a radial velocity of $\sim +15$ km s^{-1} and a Gaussian FWHM of ∼46 km s^{-1}. In contrast, the [O I] λ5577 line (single-peaked) is only seen at Φ = 0.806. The [O I] λ5577 line has a radial velocity of $\sim +130$ km s^{-1} and a Gaussian FWHM of ∼28 km s^{-1}. Even though the [O I] λ6300 and [O I] λ6364 lines originate from similar regions in terms of temperature and density (Kraus et al. 2010), we do not see the presence of the [O I] λ6364 line in any of our MIKE spectra. There are more emission lines at Φ = 0.533 than at Φ = 0.806. Here, we also see evidence for single-peaked permitted Fe II and C I and forbidden [Fe II] lines in the MIKE spectra. For example, the forbidden [Fe II] λ5269 line at $\sim +185$ km s^{-1} has a Gaussian FWHM of ∼24 km s^{-1}. In contrast, the permitted Fe II λ5265 line at $\sim +195$ km s^{-1} has a Gaussian FWHM of ∼11 km s^{-1}.

3.6 Limit on X-rays

Taken simultaneously with the *Swift* UVOT observations presented in Section 2.1, MACHO 80.7443.1718 was also observed using the *Swift* X-ray Telescope (XRT; Burrows et al. 2005). To place constraints on the presence of X-ray emission associated with this source, we reprocessed observations sw0045437001-002 and sw0045569001-002 using the *Swift* XRTPIPELINE version 0.13.2 and standard filter and screening criteria. Using a 30 arcsec source region centred on MACHO 80.7443.1718 and a 150 arcsec source-free background region located at (α_{J2000}, δ_{J2000})=(05:25:30.6787,−68:48:28.700), we find no significant X-ray emission arising from the source. To place deep constraints on the presence of X-ray emission, we combined all four observations using XSELECT version 2.4k. In this merged data set, we derive a 3σ upperlimit on the 0.3–2.0 keV count rate of 2.0×10^{-3} counts s^{-1}. Assuming $E(B-V) = 0.17$ from Section 3.2, and using the relation from Liszt (2014), the Galactic column density towards MACHO 80.7443.1718 is $N_{\rm H} \sim 1.41 \times 10^{21}$ cm^{-2}, which is consistent with the Galactic column density along the line of sight ($N_{\rm H,\,LOS} = 1.44 \times 10^{21}$ cm^{-2}; HI4PI Collaboration 2016). Assuming an absorbed power law with a photon index of 2, we derive absorbed (unabsorbed) flux of 5.0×10^{-14} erg cm^{-2} s^{-1} (8.4×10^{-14} erg cm^{-2} s^{-1}), which corresponds to an absorbed (unabsorbed) X-ray luminosity of 1.5×10^{34} erg s^{-1} (2.5×10^{34} erg s^{-1}).

4 DISCUSSION

MACHO 80.7443.1718 is by far the most extreme heartbeat discovered. In this work, we have shown that it is also one of the most massive heartbeat star systems thus known with a total mass of $M_{\rm tot} \sim 50$ M$_\odot$. We note that Kołaczek-Szymański et al. (2021) discovered that the likely hierarchical quadruple system HD 5980 in the Small Magellanic Cloud with $M_{\rm tot} \gtrsim 150$ M$_\odot$ contained a heartbeat star, making this the most massive heartbeat star system known. In comparison, ι Ori, which consists of a binary system with a O9 III primary and a B1 III-IV secondary has a total mass of $M_{\rm tot} \sim 37$ M$_\odot$ (Pablo et al. 2017). ϵ Lupi is another massive heartbeat

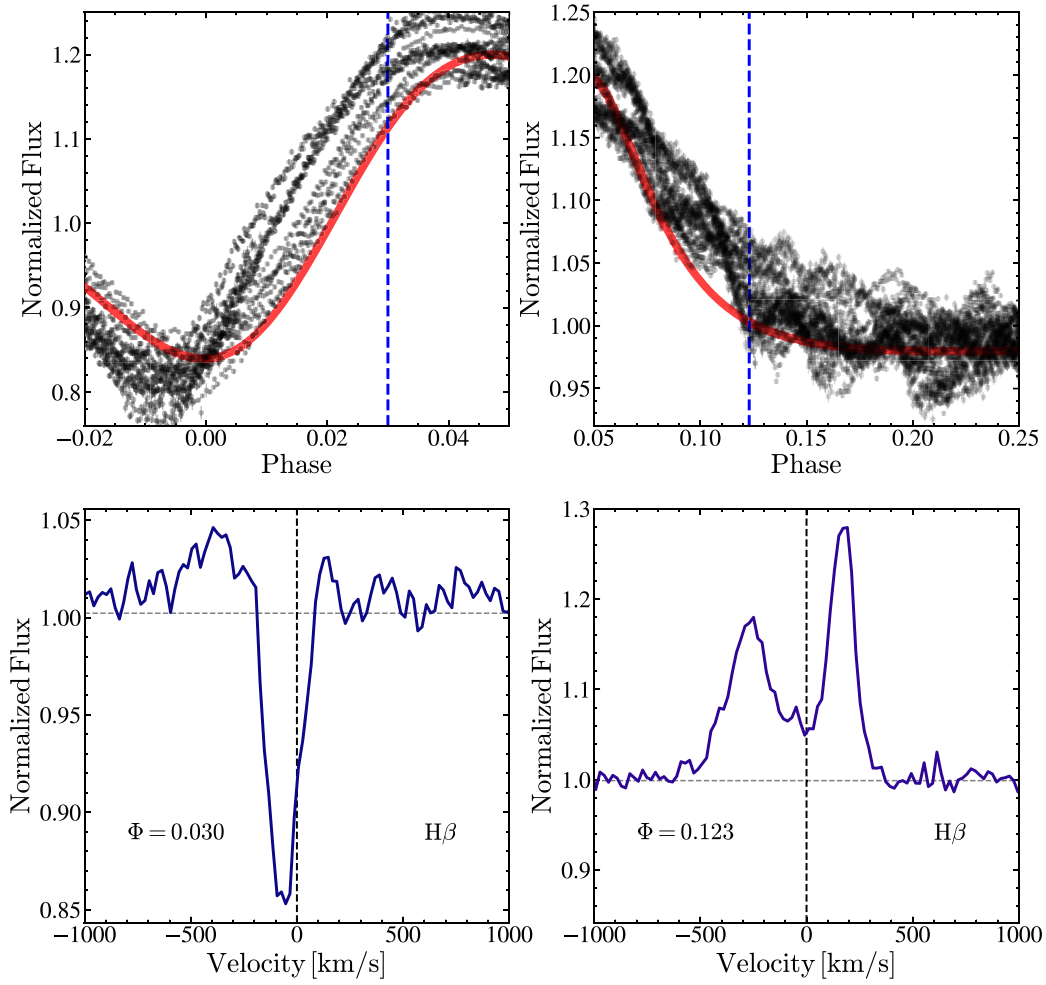

Figure 14. The *TESS* light curves (top) and SOAR Hβ line profiles (bottom) at $\Phi = 0.030$ and $\Phi = 0.123$ (vertical lines in top panels) corresponding to periastron passage and the first spectroscopic epoch with evidence of a circumstellar disc. The Kumar et al. (1995) model for tidal distortions at periastron is shown in red.

star system composed of two early-type main-sequence B stars with $M_{\rm tot} \sim 20\,{\rm M}_\odot$ (Pablo et al. 2019). MACHO 80.7443.1718 is also the only confirmed heartbeat star system consisting of a blue supergiant with a circumstellar disc.

We can understand the short disc lifetime with analytical arguments. The orbital semimajor axis from the orbital period ($P_{\rm orb}$) and Kepler's third law in terms of the stellar radius $R_* \simeq 24\,R_\odot$ is

$$a = \left(\frac{G(M_1+M_2)P_{\rm orb}^2}{4\pi^2}\right)^{1/3} = 93R_\odot\left(\frac{M_1+M_2}{10\,{\rm M}_\odot}\right)^{1/3} \simeq 159R_\odot \simeq 6.7R_*\,, \quad (7)$$

where $M_1 \simeq 34.5\,{\rm M}_\odot$ and $M_2 \simeq 15.7\,{\rm M}_\odot$. The pericentric radius $R_p = a(1-e)$ is

$$R_p \simeq 46R_\odot\left(\frac{M_1+M_2}{10\,{\rm M}_\odot}\right)^{1/3} \simeq 78R_\odot \simeq 3.3R_*. \quad (8)$$

For $q = M_1/M_2 \simeq 2.2$, $R_L/a = 0.448$, and the Roche limit is $R_L \simeq 71\,R_\odot \simeq 3.0R_*$ (Eggleton 1983). At periastron, the primary comes close to filling its Roche lobe ($R_{L,\,\rm peri} \simeq 1.5\,R_*$) with a fillout factor $f = R_*/R_{L,\,\rm peri} \simeq 0.7$. Material in a disc around the primary star will extend beyond the stellar photosphere and so, we should not be surprised to see mass transfer from the disc to the secondary star.

We can use the Hβ line to derive the radius of the Hβ emitting region using the estimate of

$$\frac{R_\beta}{R_*} \simeq \left(\frac{v\sin(i)v_{\rm crit}}{350\Delta\lambda}\right)^j \simeq \left(\frac{261}{\Delta\lambda}\right), \quad (9)$$

from Mennickent & Vogt (1991), where $v_{\rm crit}{\sim}530\,{\rm km\,s^{-1}}$, $\Delta\lambda$ is the half-peak separation in the Hβ line profile, and $j \approx 1$ is a rotation exponent. While it is not the true radius of the disc, R_β can track its evolution with orbital phase. R_β evolves from $\sim$1.2 R_* at $\Phi = 0.123$ to $\sim$2 R_* at $\Phi = 0.871$, indicating the growth of the disc after periastron passage. In the spectra taken before periastron at $\Phi = 0.905$ and at $\Phi = 0.998$, this drops to $R_\beta \sim 1.4\,R_*$, which suggests that the disc starts to shrink as the two stars approach each other. Hβ is in emission at $\Phi = 0.998$ but at $\Phi = 0.030$, Hβ is in absorption and shows little evidence for a disc (see Fig. 12). Thus, in the span of $\sim$4 h the disc around MACHO 80.7443.1718 appears to dissipate. At periastron, a disc beyond a radius $R_d > R_{L,\,\rm peri} \simeq 1.5R_*$ will result in mass transfer to the secondary. Given that the discs around Be stars are larger than a few R_*, it is very likely that mass transfer occurs at periastron in this system. However, this framework is complicated by the tidal interactions exerted on the disc by the secondary.

To obtain a rough estimate of the stability of the disc during a pericentric passage, we used the approach of Kochanek (1993). We

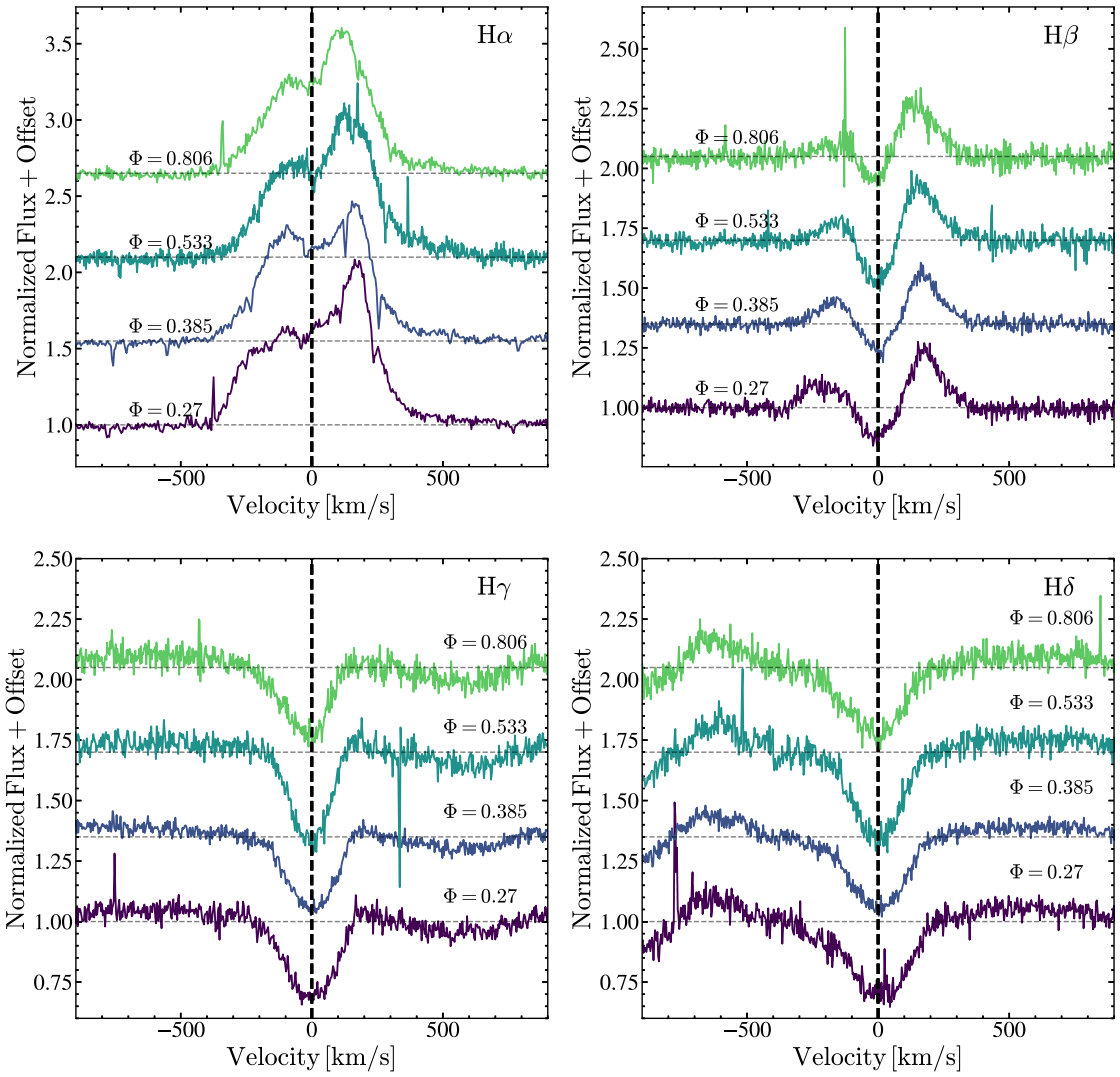

Figure 15. MIKE line profiles for Hα, Hβ, Hγ, and Hδ sorted by phase.

set-up the stars at apocentre with their nominal masses, put a ring of test particles in circular orbits around the Be star, and then followed their evolution through one orbit. As a simple metric for the stability of the disc as a function of radius, we simply examined the maximum and minimum radii of the test particles at the end and the fraction still bound to the Be star. Material closer than 30 $R_\odot$ likely can remain in a disc. For example, at 30 $R_\odot$ ring ends up with a radial spread from 19.8 to 36.4 $R_\odot$ with all particles bound. At 25 $R_\odot$, the radial range shrinks from 22.6 to 26.6 $R_\odot$. At 35 $R_\odot$, the particles are still bound but the radial range has expanded from 4.6 to 47.4 $R_\odot$. More distant rings are significantly disrupted. At 40 and 45 $R_\odot$, the outer radius is ∼280 $R_\odot$ and the bound fractions are 83 per cent and 72 per cent, respectively. While crude, this experiment suggests that only the very inner portions of the disc can survive a pericentric encounter.

Be stars in eccentric binaries can actually have increased mass-loss rates due to binary interactions. At periastron, the secondary component can trigger outbursts in the Be star due to tidal forces that depend on the stellar properties of the Be star and the configuration of the binary orbit (Labadie-Bartz et al. 2017). The role of binary interactions in triggering Be outbursts has been studied with the Be star δ Sco which is in a highly eccentric ($e = 0.94 \pm 0.01$) orbit with $P_{\rm orb} \sim 10.6$ yr (Miroshnichenko et al. 2003). Spectroscopic observations of δ Sco at periastron passage suggest an increase in the mass-loss rate at periastron (Miroshnichenko et al. 2001). It has been suggested that non-radial pulsations are amplified at periastron, resulting in an increased mass-loss rate (Miroshnichenko et al. 2001). In the case of MACHO 80.7443.1718, we have significant evidence for high-amplitude TEOs following periastron passage, along with photometric and spectroscopic evidence of outbursts immediately (∼4 d) following periastron (see Fig. 14). This provides strong evidence for amplified non-radial pulsations at periastron triggering mass-loss in MACHO 80.7443.1718.

Given that both the components of this system are fairly massive and on a close orbit, this system maybe useful for studying the role of binary interactions in the formation of compact objects. We evolved a model of this system with the `COSMIC` binary population synthesis model, assuming the default prescriptions in Breivik et al. (2020). The BPS models show that the primary will undergo Roche lobe overflow as it evolves, increasing the mass of the secondary to ∼24 $M_\odot$. Following mass transfer, the primary will end up on the He main sequence with ∼12 $M_\odot$. Subsequently, the primary undergoes a supernova explosion, resulting in the formation of a bound black hole of mass $M_{\rm BH} \sim 8$ $M_\odot$. The secondary evolves and forms a He main-sequence star with ∼7 $M_\odot$. Following the supernova of the

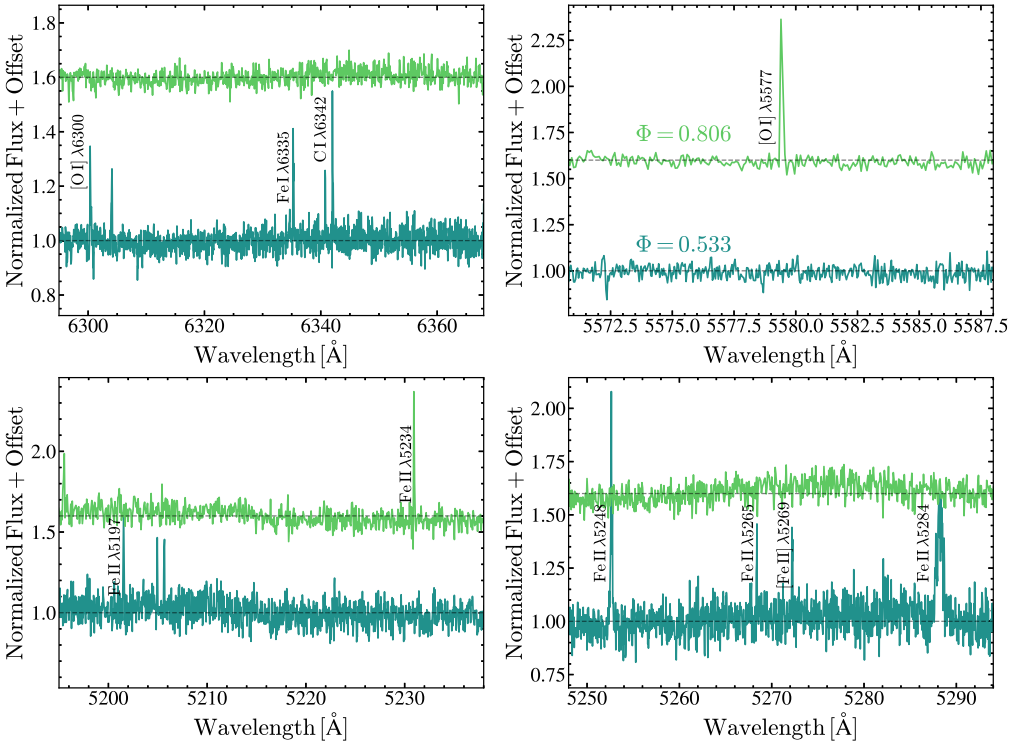

Figure 16. MIKE spectra at $\Phi = 0.533$ and $\Phi = 0.806$ indicating the presence of O I, C I, Fe II, [O I], and [Fe II] emission lines.

secondary star, it will form a neutron star of mass $M_{\rm NS} \sim 1.6\,{\rm M}_{\odot}$, and the binary is disrupted.

5 CONCLUSIONS

Using *TESS* photometry and spectroscopic observations from MIKE and SOAR, we have studied the extreme LMC heartbeat star MACHO 80.7443.1718. We find that:

(i) MACHO 80.7443.1718 is a heartbeat star with the most extreme brightness variations observed to date. The ASAS-SN and *TESS* light curves show photometric variations of ∼40 per cent at periastron due to tidal distortions and variations of ∼10 per cent due to TEOs outside periastron.

(ii) MACHO 80.7443.1718 is a massive binary on a short period ($P_{\rm orb} = 32.83627 \pm 0.00846$ d), eccentric ($e = 0.507 \pm 0.033$) orbit, composed of a B0 Iae supergiant with $M_1 \simeq 34.5\,{\rm M}_{\odot}$ and a O9.5V secondary with $M_2 \simeq 15.4\,{\rm M}_{\odot}$. Thus, this system is among the most massive heartbeat systems yet discovered.

(iii) If MACHO 80.7443.1718 is co-eval with the LH58 OB association, the CMD of the association also implies an age of ∼6 Myr old.

(iv) MACHO 80.7443.1718 is likely a B[e] supergiant, showing emission in the Balmer lines and other permitted/forbidden emission lines from metals like O and Fe. However, we do not identify the strong NIR excess that is typical for these objects.

(v) MACHO 80.7443.1718 contains a circumstellar disc that disappears and then reforms at each periastron passage. We see significant *V*/*R* variability in the Balmer emission-line profiles during an orbit. The disc rapidly dissipates at periastron which could indicate mass transfer to the secondary but re-emerges immediately after.

(vi) MACHO 80.7443.1718 shows evidence for TEOs at $N = 25$ and $N = 41$ which likely correspond to the $(l, m) = (2, 0)$ and $(l, m) = (2, |2|)$ modes, respectively. We also retrieved a frequency that is very similar to the expected rotation period of the primary star.

To fully understand the complex behaviour of this system, detailed models that consider the interaction of the circumstellar disc with the stellar components are necessary. Our results have provided useful clues at understanding this unique binary and have shown that this system is not just unusual because of its unprecedented variability amplitudes but that it is also one of the most massive heartbeat stars known with a B[e] supergiant. Therefore, MACHO 80.7443.1718 is an excellent astrophysical laboratory to study not just the binary interactions amongst massive stars but also their evolution and mass-loss properties.

ACKNOWLEDGEMENTS

We thank Dr. Jim Fuller for useful discussions on this system and for comments on the manuscript. ASAS-SN is supported by the Gordon and Betty Moore Foundation through grant GBMF5490 to the Ohio State University, and NSF grants AST-1515927, AST-1814440, and AST-1908570. Development of ASAS-SN has been supported by NSF grant AST-0908816, the Mt. Cuba Astronomical Foundation, the Center for Cosmology and AstroParticle Physics at the Ohio State University, the Chinese Academy of Sciences South America Center for Astronomy (CAS- SACA), the Villum Foundation, and George Skestos. TJ acknowledges support from the Ohio State Presidential Fellowship. KZS and CSK are supported by NSF grants AST-1515927, AST-1814440, and AST-1908570. JS acknowledges support from the Packard Foundation. JTH was supported by NASA award 80NSSC21K0136. BJS is supported by NSF grants AST-1908952, AST-1920392, and AST-1911074. Support for JLP is provided in part by the Ministry of Economy, Development, and Tourism's Millennium Science Initiative through grant IC120009, awarded to The Millennium Institute of

Astrophysics, MAS. EA acknowledges NSF award AST-1751874, NASA awards 11-Fermi 80NSSC18K1746, 13-Fermi 80NSSC20K1535, and 16-Swift 80NSSC21K0173, and a Cottrell fellowship of the Research Corporation. KCD acknowledges funding from the McGill Space Institute, the Natural Sciences and Engineering Research Council of Canada (NSERC), and the McGill Bob Wares Science Innovation Prospectors Fund. Parts of this research were supported by the Australian Research Council Centre of Excellence for All Sky Astrophysics in 3 Dimensions (ASTRO 3D), through project number CE170100013. Based on observations obtained at the Southern Astrophysical Research (SOAR) telescope, which is a joint project of the Ministério da Ciência, Tecnologia e Inovações (MCTI/LNA) do Brasil, the US National Science Foundation's NOIRLab, the University of North Carolina at Chapel Hill (UNC), and Michigan State University (MSU). This research has made use of the VizieR catalogue access tool, CDS, Strasbourg, France. This research also made use of ASTROPY, a community-developed core PYTHON package for Astronomy (Astropy Collaboration 2018).

DATA AVAILABILITY

The data underlying this article will be shared on reasonable request to the corresponding author.

REFERENCES

Adams S. M., Kochanek C. S., 2015, MNRAS, 452, 2195
Alard C., 2000, A&AS, 144, 363
Alard C., Lupton R. H., 1998, ApJ, 503, 325
Alcock C. et al., 1997, ApJ, 486, 697
Astropy Collaboration et al., 2018, AJ, 156, 123
Bagnulo S., Jehin E., Ledoux C., Cabanac R., Melo C., Gilmozzi R., ESO Paranal Science Operations Team, 2003, Messenger, 114, 10
Barclay T., 2017, tessgi/ticgen: v1.0.0
Bernstein R., Shectman S. A., Gunnels S. M., Mochnacki S., Athey A. E., 2003, in Iye M., Moorwood A. F. M., eds, Proc SPIE Conf. Ser. Vol.4841, Instrument Design and Performance for Optical/Infrared Ground-based Telescopes. SPIE, Bellingham, p. 1694
Borucki W. J. et al., 2010, Science, 327, 977
Bragança G. A., Daflon S., Cunha K., Bensby T., Oey M. S., Walth G., 2012, AJ, 144, 130
Breeveld A. A. et al., 2010, MNRAS, 406, 1687
Breivik K. et al., 2020, ApJ, 898, 71
Burrows D. N. et al., 2005, Space Sci. Rev., 120, 165
Cardelli J. A., Clayton G. C., Mathis J. S., 1989, ApJ, 345, 245
Castelli F., Kurucz R. L., 2003, in Piskunov N., Weiss W. W., Gray D. F., eds, Proc. IAU Symp. 210, Modelling of Stellar Atmospheres. Kluwer, Dordrecht, p. A20
Cheng S. J., Fuller J., Guo Z., Lehman H., Hambleton K., 2020, ApJ, 903, 122
Choi J., Dotter A., Conroy C., Cantiello M., Paxton B., Johnson B. D., 2016, ApJ, 823, 102
Choudhury S., Subramaniam A., Cole A. A., 2016, MNRAS, 455, 1855
Cioni M. R. et al., 2000, A&AS, 144, 235
Clemens J. C., Crain J. A., Anderson R., 2004, in Moorwood A. F. M., Iye M., eds, Proc. SPIE Conf. Ser. Vol. 5492, Ground-Based Instrumentation for Astronomy. SPIE, Bellingham, p. 331
Conti P. S., Alschuler W. R., 1971, ApJ, 170, 325
Cutri R. M. et al., 2003, VizieR Online Data Catalog, p. II/246
Dotter A., 2016, ApJS, 222, 8
Eastman J., Siverd R., Gaudi B. S., 2010, PASP, 122, 935
Eggleton P. P., 1983, ApJ, 268, 368
Elitzur M., Ivezić Ž., 2001, MNRAS, 327, 403
Foreman-Mackey D., Hogg D. W., Lang D., Goodman J., 2013, PASP, 125, 306
Fuller J., 2017, MNRAS, 472, 1538
Garmany C. D., Massey P., Parker J. W., 1994, AJ, 108, 1256
Guo Z., Shporer A., Hambleton K., Isaacson H., 2020, ApJ, 888, 95
Hagen L. M. Z., Siegel M. H., Hoversten E. A., Gronwall C., Immler S., Hagen A., 2017, MNRAS, 466, 4540
Hambleton K. et al., 2018, MNRAS, 473, 5165
HI4PI Collaboration, 2016, A&A, 594, A116
Horvat M., Conroy K. E., Pablo H., Hambleton K. M., Kochoska A., Giammarco J., Prša A., 2018, ApJS, 237, 26
Howell S. B. et al., 2014, PASP, 126, 398
Hummel W., Vrancken M., 1995, A&A, 302, 751
Ivezic Z., Elitzur M., 1997, MNRAS, 287, 799
Jayasinghe T. et al., 2018, MNRAS, 477, 3145
Jayasinghe T. et al., 2019a, MNRAS, 486, 1907
Jayasinghe T., Stanek K. Z., Kochanek C. S., Thompson T. A., Shappee B. J., Fausnaugh M., 2019b, MNRAS, 489, 4705
Johnson H. L., 1958, Lowell Obs. Bull., 4, 37
Kelson D. D., 2003, PASP, 115, 688
Kelson D. D., Illingworth G. D., van Dokkum P. G., Franx M., 2000, ApJ, 531, 184
Kirk B. et al., 2016, AJ, 151, 68
Kochanek C. S. et al., 2017, PASP, 129, 104502
Kochanek C. S., 1993, ApJ, 406, 638
Kołaczek-Szymański P. A., Pigulski A., Michalska G., Moździerski D., Różański T., 2021, A&A, 647, A12
Kraus M., 2019, Galaxies, 7, 83
Kraus M., Borges Fernandes M., de Araújo F. X., 2010, A&A, 517, A30
Kumar P., Ao C. O., Quataert E. J., 1995, ApJ, 449, 294
Labadie-Bartz J. et al., 2017, AJ, 153, 252
Lamers H. J. G. L. M., Zickgraf F.-J., de Winter D., Houziaux L., Zorec J., 1998, A&A, 340, 117
Lanz T., Hubeny I., 2003, ApJS, 146, 417
Lanz T., Hubeny I., 2007, ApJS, 169, 83
Lenz P., Breger M., 2005, Commun. Asteroseismol., 146, 53
Liszt H., 2014, ApJ, 780, 10
Maíz Apellániz J. et al., 2013, Massive Stars: From Alpha to Omega. p.198
Martins F., 2018, A&A, 616, A135
Martins F., Schaerer D., Hillier D. J., 2005, A&A, 436, 1049
Massey P., 2002, ApJS, 141, 81
Massey P., Garmany C. D., Silkey M., Degioia-Eastwood K., 1989, AJ, 97, 107
Mathys G., 1988, A&AS, 76, 427
Meixner M. et al., 2006, AJ, 132, 2268
Mennickent R. E., Vogt N., 1991, A&A, 241, 159
Miglio A., Montalbán J., Dupret M.-A., 2007, MNRAS, 375, L21
Miroshnichenko A. S. et al., 2001, A&A, 377, 485
Miroshnichenko A. S. et al., 2003, A&A, 408, 305
Negueruela I., Reig P., Finger M. H., Roche P., 2000, A&A, 356, 1003
Pablo H. et al., 2017, MNRAS, 467, 2494
Pablo H. et al., 2019, MNRAS, 488, 64
Paxton B. et al., 2013, ApJS, 208, 4
Paxton B. et al., 2015, ApJS, 220, 15
Paxton B., Bildsten L., Dotter A., Herwig F., Lesaffre P., Timmes F., 2011, ApJS, 192, 3
Pietrzyński G. et al., 2013, Nature, 495, 76
Poole T. S. et al., 2008, MNRAS, 383, 627
Price-Whelan A. M., Hogg D. W., Foreman-Mackey D., Rix H.-W., 2017, ApJ, 837, 20
Prša A. et al., 2016, ApJS, 227, 29
Quirrenbach A. et al., 1997, ApJ, 479, 477
Ricker G. R. et al., 2015, J. Astron. Telesc. Instrum. Syst., 1, 014003
Rivinius T., Carciofi A. C., Martayan C., 2013, A&A Rev., 21, 69
Roming P. W. A. et al., 2005, Space Sci. Rev., 120, 95
Shappee B. J. et al., 2014, ApJ, 788, 48
Sota A., Maíz Apellániz J., Morrell N. I., Barbá R. H., Walborn N. R., Gamen R. C., Arias J. I., Alfaro E. J., 2014, ApJS, 211, 10

Sota A., Maíz Apellániz J., Walborn N. R., Alfaro E. J., Barbá R. H., Morrell N. I., Gamen R. C., Arias J. I., 2011, ApJS, 193, 24
Stassun K. G. et al., 2018, AJ, 156, 102
Sterken C., Vogt N., Mennickent R. E., 1996, A&A, 311, 579
Strader J., Chomiuk L., Sonbas E., Sokolovsky K., Sand D. J., Moskvitin A. e. S., Cheung C. C., 2014, ApJ, 788, L27
Thompson S. E. et al., 2012, ApJ, 753, 86
Vallely P. J., Kochanek C. S., Stanek K. Z., Fausnaugh M., Shappee B. J., 2020, MNRAS, 500, 5639
Walborn N. R., Fitzpatrick E. L., 1990, PASP, 102, 379
Wright E. L. et al., 2010, AJ, 140, 1868
Zaritsky D., Harris J., Thompson I. B., Grebel E. K., 2004, AJ, 128, 1606
Zickgraf F. J., 2006, in Kraus M., Miroshnichenko A. S., eds, ASP Conf. Ser. Vol. 355, Stars with the B[e] Phenomenon. Astron. Soc. Pac., San Francisco, p. 135

This paper has been typeset from a TEX/LATEX file prepared by the author.